metals

MDPI

Article

Combining Digital Twin and Machine Learning for the Fused Filament Fabrication Process

Javaid Butt * and Vahaj Mohaghegh

Faculty of Science and Engineering, Anglia Ruskin University, Chelmsford CM1 1SQ, UK
* Correspondence: javaid.butt@aru.ac.uk

Abstract: In this work, the feasibility of applying a digital twin combined with machine learning algorithms (convolutional neural network and random forest classifier) to predict the performance of PLA (polylactic acid or polylactide) parts is being investigated. These parts are printed using a low-cost desktop 3D printer based on the principle of fused filament fabrication. A digital twin of the extruder assembly has been created in this work. This is the component responsible for melting the thermoplastic material and depositing it on the print bed. The extruder assembly digital twin has been separated into three simulations, i.e., conjugate convective heat transfer, multiphase material melting, and non-Newtonian microchannel. The functionality of the physical extruder is controlled by a PID/PWM circuit, which has also been modelled within the digital twin to control the virtual extruder's operation. The digital twin simulations were validated through experimentation and showed a good agreement. After validation, a variety of parts were printed using PLA at four different extrusion temperatures (180 °C, 190 °C, 200 °C, 210 °C) and ten different extrusion rates (ranging from 70% to 160%). Measurements of the surface roughness, hardness, and tensile strength of the printed parts were recorded. To predict the performance of the printed parts using the digital twin, a correlation was established between the temperature profile of the non-Newtonian microchannel simulation and the experimental results using the machine learning algorithms. To achieve this objective, a reduced order model (ROM) of the extruder assembly digital twin was developed to generate a training database. The database generated by the ROM (simulation results) was used as the input for the machine learning algorithms and experimental data were used as target values (classified into three categories) to establish the correlation between the digital twin output and performance of the physically printed parts. The results show that the random forest classifier has a higher accuracy compared to the convolutional neural network in categorising the printed parts based on the numerical simulations and experimental data.

Keywords: digital twin; fused filament fabrication; machine learning; random forest classifier; convolutional neural network

check for updates

Citation: Butt, J.; Mohaghegh, V. Combining Digital Twin and Machine Learning for the Fused Filament Fabrication Process. *Metals* **2023**, *13*, 24. https://doi.org/10.3390/met13010024

Academic Editors: Eric Hug and Xudong Qian

Received: 25 October 2022
Revised: 23 November 2022
Accepted: 15 December 2022
Published: 22 December 2022

Copyright: © 2022 by the authors. Licensee MDPI, Basel, Switzerland. This article is an open access article distributed under the terms and conditions of the Creative Commons Attribution (CC BY) license (https://creativecommons.org/licenses/by/4.0/).

1. Introduction

The benefits of additive manufacturing (AM) methods cannot be overstated, as they range from design freedom and reduced lead times to cost-effectiveness and customisation [1–3]. However, despite such innovative features, AM methods also suffer from poor surface finishes and structural integrity, which limit their applicability as well as their adoptability [4–7]. Due to the capability of AM methods to work with different materials (e.g., metal, thermoplastics, ceramics), there is a need for an optimisation of the process parameters to achieve the desired results. This is a challenging task due to the interrelationship among such process parameters, and modifying one can adversely affect the required properties of the products [8–10]. For example, metal parts made by AM methods (e.g., direct metal laser sintering, electron beam melting) suffer from porosity and brittleness and are prone to shrinkage if the operating parameters (e.g., laser power, spot size, scanning speed, layer

thickness) are not properly optimised. In addition, such methods produce a considerable degree of waste while featuring high purchasing and operating costs [11–14]. On the other hand, there is a popular AM method with affordable raw material and operation/maintenance costs called fused filament fabrication (FFF) of fused deposition modelling (FDM). This method utilises thermoplastics as raw material extruded out of a heated nozzle and is one of the most used AM methods on the market. It offers several advantages, such as ease of operation, a wide variety of available materials, fast printing speeds, and affordability [15,16]. Despite these notable benefits, FFF also suffers from poor surface finish and mechanical properties [17]. The challenge is the optimisation of the process parameters (such as layer height, line width, nozzle temperature, print bed temperature, deposition speed) that directly influence the products. Furthermore, failed prints may occur for several reasons. They include but are not limited to motor stall, nozzle blockage, bearing failure, timing belt breakage, abnormal extrusion, and the detachment of items from the print bed [18]. These occurrences lead to a significant wastage of the raw material [19], and the most common way to mitigate this issue is by using the trial-and-error method. However, this is extremely time-consuming and is accompanied by an elevated number of expenses. Therefore, there has been an increased focus on the use of sensors [20] for temperature distribution [21], extrusion nozzle flow rate [22], and layer adhesion [23]. Moreover, numerical methods such as the finite element method, finite difference method, and finite volume method are widely used to perform heat and fluid flow simulations [24–26]. These simulations can provide results based on the applied boundary conditions and can be further augmented using artificial intelligence (AI) and machine learning (ML) to provide useful information to the users [27].

ML is considered a subset of AI [28] and can be further subdivided into the categories of supervised learning, unsupervised learning, and reinforcement learning. It is to be noted that most of the ML methods used in AM applications are supervised methods [29]. Such applications yield large datasets that can enhance the performance of the ML algorithms. Despite the benefits of ML in different domains, its results are highly dependent on the features extracted from the training datasets. Therefore, deep learning algorithms (a subcategory of ML), which automatically extract higher-level features from the raw input data, became exceeding popular. Deep learning algorithms are based on artificial neural networks (ANN), and, among their methods, the convolutional neural network (CNN) algorithm is the most widely used [30]. Furthermore, other ML methods such as random forest (RF) have also shown promising results while estimating the properties of parts made by AM methods [31].

The incorporation of ML is quite useful for simulations. However, this still does not solve the significant issue of providing control. Numerical simulations are devoid of a control model and will stop mimicking reality once a specified condition is achieved. For example, the extruder of a fused filament fabrication system is typically set at a specified temperature as per the material being used. The control circuit, using sensors, tells the system to increase the temperature up to the specified value and maintain it for the duration of the print. In this context, a new scientific approach with the control model has emerged and is called a digital twin (DT). It is defined as a dynamic virtual copy of a physical asset, process, system, or environment that looks like and behaves identically to its real-world counterpart. A digital twin can be used to run simulations before actual devices are built and deployed. Digital twins can also take real-time sensor data and apply AI as well as data analytics to optimize performance. They can be model driven [32] or data driven [33] and can help with the optimization of process parameters as well as improved asset management/performance, leading to significant savings in comparison with the costs that would commonly be incurred while following the trial-and-error method [34–36].

The use of ML algorithms is also extremely beneficial for interpreting the data gathered using AM methods and can help researchers to make informed decisions. Kumar et al. [37] proposed a low-cost multi-sensor data acquisition system for detecting various faults in FDM-printed parts. They performed time and frequency domain analyses on captured

data to create feature vectors by selecting the chi-square method, and the most significant features were selected to train the CNN model, which gave an accuracy of around 94%. Alejandrino et al. [38] proposed an ANN-based model for a novel lattice infill pattern in FDM. For ABS material, their model resulted in 98.8% accuracy during network training and the new infill pattern could save material up to 61.3% compared to conventional infill patterns. Banadaki et al. [39] developed a CNN-based methodology for in-situ quality monitoring and control in FDM with the model showing an accuracy of 94%. Wu et al. [40] presented a data fusion approach for surface roughness prediction in FDM parts. They trained the predictive models using random forests, support vector regression, ridge regression, and least absolute shrinkage and selection operator. Their experimental results have shown that the predictive models trained by the ML algorithms can predict the surface roughness of FDM-printed parts with very high accuracy. Hooda et al. [41] investigated the effects of deposition angle using different shapes/geometries and employed correlation-based feature selection technique to explore the crucial features of the FDM-printed parts. They performed prediction and validation using ensemble-based random forest machine learning model that showed a prediction accuracy of 94.57%. Barrios and Romero [42] compared the performance of three decision tree algorithms (C4.5, random tree, and random forest) in predicting surface roughness of FDM-printed parts and found that random tree performed best with a classification accuracy as high as 86.67%.

The development of a functional DT for AM requires validation of the results against experimentation to ensure its efficacy. For example, Mourtzis et al. [43] developed a framework for monitoring and optimizing the parameters of FDM based on the utilization of DT and cloud technology. The demonstrated the use of a mobile application that can run offline as well as online simulations. They also developed graphical user interfaces based on augmented reality that help in the remote operation and monitoring of the FDM system. Balta et al. [44] presented a DT framework for real-time performance monitoring and anomaly detection in FDM using process measurement data with continuous and discrete event dynamics, thus providing additional monitoring and analysis capabilities to the physical FDM system. Osho et al. [45] described the design of a 4 Rs (Representation, Replication, Reality, and Relational) framework for creating a general purpose and modular DT for FDM. They implemented the DT via temperature as well as position sensors and demonstrated its scalability. Corradini et al. [46] presented a multifunctional DT model of an FFF 3D printer using smart sensors that collected data about the actual operation of the printer and compared them with the simulated model, thus enabling real-time monitoring of the printing process.

It is clear from the literature that digital twins are the future of manufacturing, and the use of AI/ML is extremely useful for obtaining better results. Therefore, this paper presents a digital twin for a low-cost, desktop-based fused filament fabrication system. Specifically, the extruder assembly has been modelled to provide data based on the input parameters. The next section describes the FFF process and the digital twin flow of activities, while the methodology is described in Section 3, along with descriptions of the reduced order modelling and machine learning development. Section 4 presents the validation results of the digital twin simulations, followed by reduced order modelling for the generation of a database and the implementation of the machine learning algorithms for the performance classification of the FFF-printed parts. Our conclusions are described in Section 5 with the practical implications of this work.

2. Description of the Fused Filament Fabrication Process

FFF is one of the most widely used AM methods on the market for working with thermoplastics. It is an extrusion-based technology in which the filament material is fed through a heated extruder and deposited onto a print bed. In this work, an Anet® ET4 Pro (Shenzen Anet Technology Company, Hong Kong, China) 3D printer was used as shown in Figure 1. The 3D printer comprises a build volume of 220 mm × 220 mm × 250 mm (X × Y × Z) and an extruder nozzle diameter of 0.4 mm. The extruder assembly is shown

in Figure 1b (physical model) and Figure 1c (CAD model), while the CAD model of the extruder is shown in Figure 1d. To manufacture a part, a CAD file (in stl format) is sent to a slicing software (e.g., Ultimaker Cura, Slic3r, PrusaSlicre) that converts the file into a series of cross-sections. They are subsequently transformed into g-codes for the 3D printer, and then the layer-by-layer construction of the part takes place. For the construction/printing, different process parameters (e.g., nozzle temperature, print bed temperature, print speed, infill percentage) must be selected. Once the selection is made, the filament is then fed to the extruder with a constant feed rate at room temperature and gradually melts as it gets to the heating block of the system. The heat is generated inside the heating element using a 40 W ceramic cartridge heater and then conducted to the rest of the components over time. The conduction subsequently melts the filament inside the heating block. To prevent the printer from overflowing/over extruding due to excessive heating, the heat sink cools down the filament on top of the heating block using a 40 mm diameter axial fan. The extruder system maintains a constant temperature by setting a fixed fan speed of 5000 rpm (100% speed) and controlling the ceramic heater with a PID/PWM circuit. This control circuit is responsible for keeping the temperature constant to allow for a print to be made. This work aims to develop and deploy a digital twin for the extruder assembly of the Anet® ET4 Pro 3D printer (Figure 1b) to successfully determine the optimal process parameters for a given filament material while maximising the performance of the printed parts. A flow chart is shown in Figure 2 describing the activities and features associated with the digital twin.

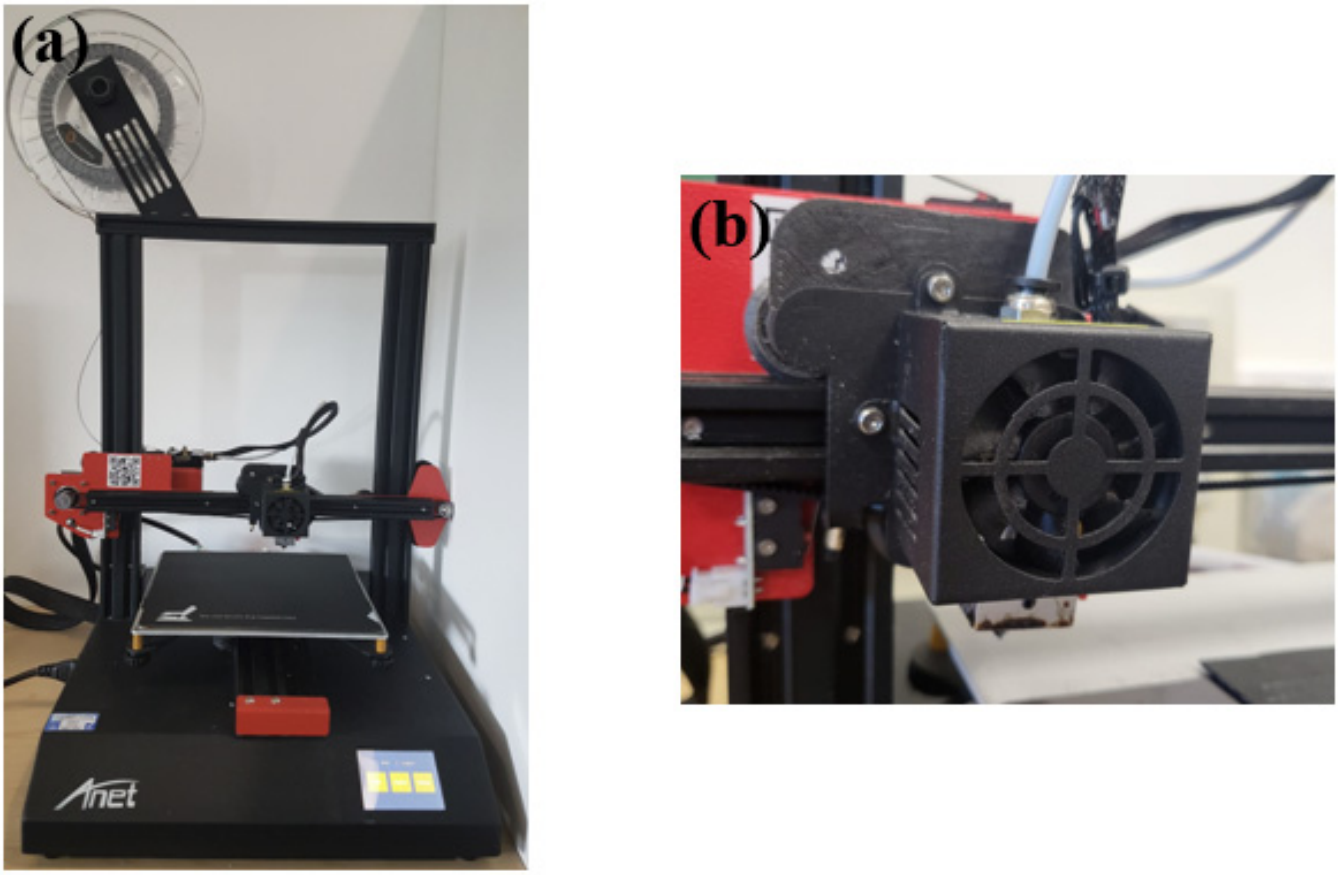


Figure 1. *Cont.*

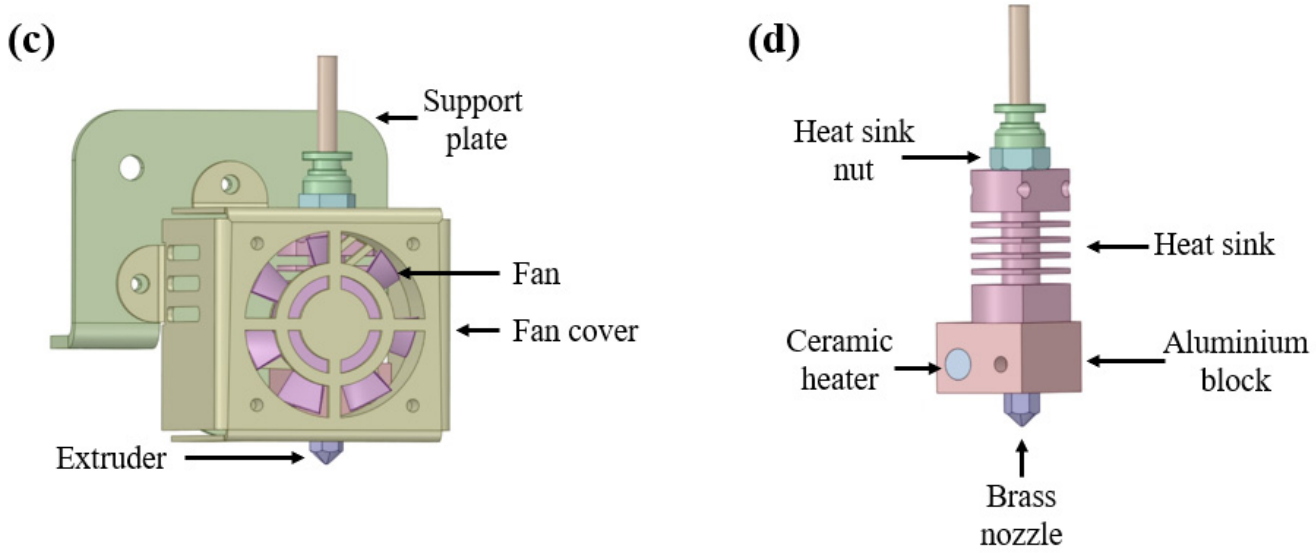


Figure 1. Anet® ET4 Pro 3D printer: (**a**) Physical 3D printer; (**b**) Physical extruder assembly; (**c**) 3D model of the extruder assembly; (**d**) 3D model of the extruder.

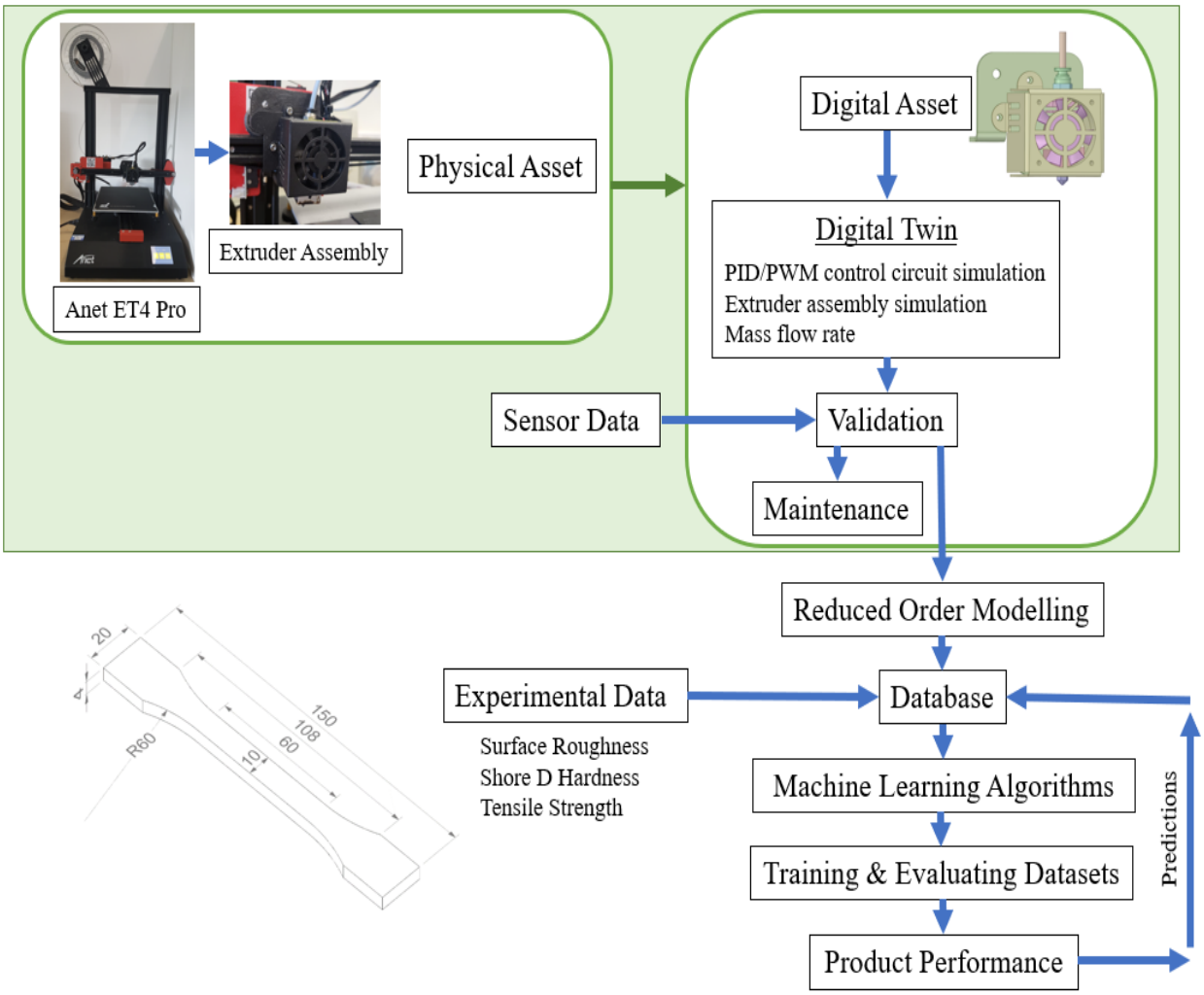


Figure 2. Flow chart of the digital twin operation.

3. Methods and Materials

An Anet® ET4 Pro 3D printer was used in this work, and dog-bone samples, according to BS EN ISO 527-2: 2012 [47], were printed using PrimaValue™ PLA (Prima Creator, Malmö, Sweden) [48]. The dimensions of the sample are shown in Figure 3 and the process parameters are shown in Table 1. Based on these parameters, the printing process was simulated using ANSYS 2021 R1, and, to develop a simulation-based digital twin in the form of an integrated multidomain system simulation, ANSYS Twin Builder was used.

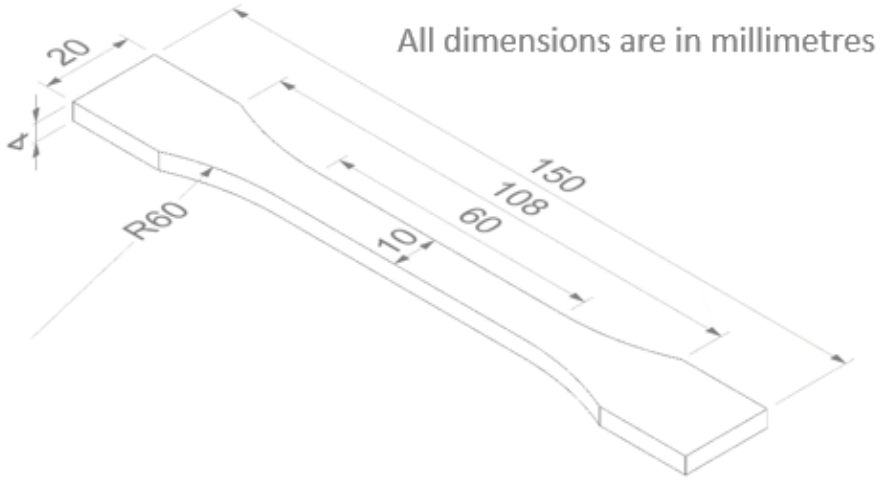


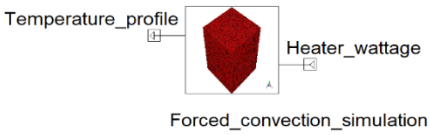
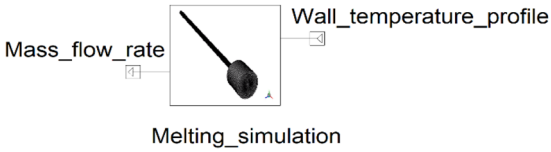
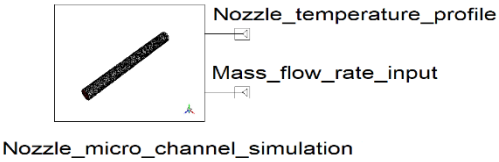
Figure 3. Dimensions of the dog-bone sample.

Table 1. Process parameters for PLA printing.

#	Parameters	Description
1	Infill density (%)	100
2	Infill pattern	Lines
3	Layer height (mm)	0.2
4	Layer width (mm)	0.6
5	Nozzle size (mm)	0.4
6	Flow (%)	100
7	Feed rate (mm/s)	8
8	Extrusion temperature (°C)	200
9	Print bed temperature (°C)	60
10	Deposition speed (mm/s)	50
11	Fan speed (%)	100

Based on the functionality of the FFF process, the extruder temperature control equivalent circuit model (ECM) is coupled with computational fluid dynamics models of conjugate convective heat transfer, a multiphase melting simulation, and a microchannel non-Newtonian flow simulation. ANSYS Fluent offers a variety of built-in tools for this type of coupled analysis. The extruder temperature control ECM was recreated in ANSYS Twin Builder, and the Fluent models were imported through three functional mock-up units (FMU). Each FMU has a series of inputs and outputs as described in Table 2. While running the simulations, each FMU is processed in a separate computational server with the Twin Builder as the host for sharing the information/data. In this way, the FMUs were coupled with each other and the ECM model to run a co-simulation, creating a digital twin for the extruder assembly as shown in Figure 4.

Table 2. Inputs and outputs for the functional mock-up units.

#	Functional Mock-Up Units	Description
1		**Forced convection heat transfer** Input: Heater wattage ON/OFF signal from the PWM module. Output: Temperature profile on the PLA boundary.
2		**PLA melting and deposition** Input: Temperature profile on the PLA boundary, feed rate and infill extrusion rate percentage. Output: PLA mass flow rate and temperature inside the extruder nozzle.
3		**Extruder nozzle microchannel** Input: Temperature profile on the PLA boundary, mass flow rate and temperature of melted PLA. Output: Mass flow rate of the PLA inside the nozzle.

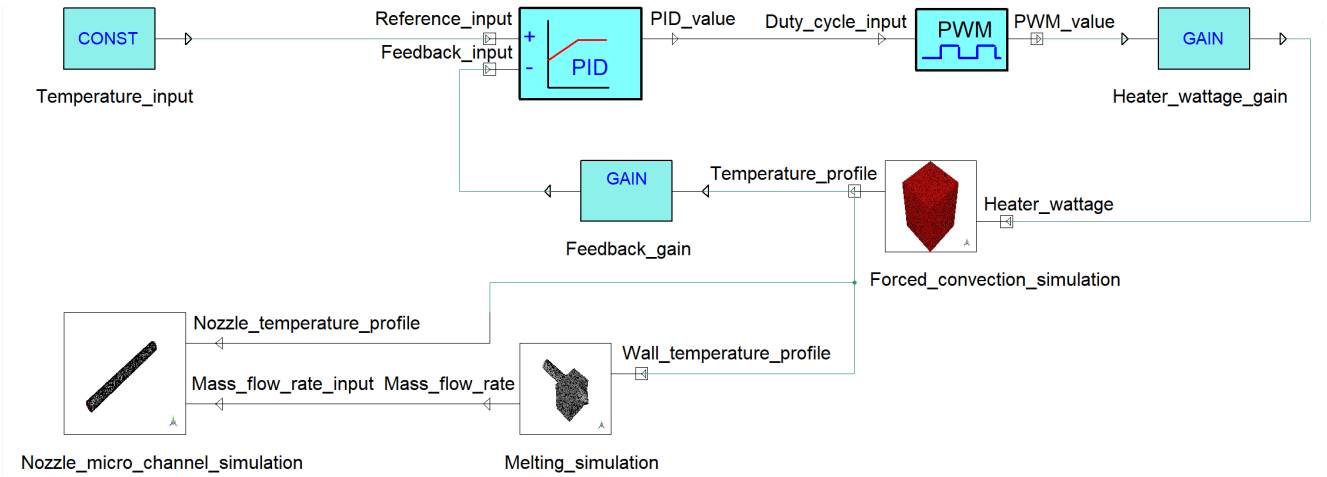


Figure 4. Digital twin layout with the ECM and the FMUs in ANSYS twin builder.

Based on Table 2 and Figure 4, the development of the ECM and the FMUs for the digital twin is separated into two distinct phases. The first phase comprises the modelling of the PID/PWM control circuit, and the second phase involves the numerical simulation of the heat transfer and fluid flow in the extruder assembly.

The digital twin of the extruder assembly is a virtual replica of the physical extruder assembly with a control model. Its purpose is to provide the user with quantitative data in the form of simulations that can be further used for maintenance operations and to ensure the smooth running of the extruder without jamming/clogging. To enhance the functionality of the digital twin from asset management to product performance improvements, reduced order modelling (Section 4.3) has been utilised. Its purpose is to accelerate the simulation run time and create a database. The database also requires experimental data for the development of the machine learning algorithms. For this purpose, dog-bone samples were physically manufactured according to BS EN ISO 527-2:2012 [47]. The 3D CAD models of the samples to be built were sent to the open-source software Ultimaker Cura 5.2.1 [49] to generate G-code files. Four different extrusion temperatures (180 °C, 190 °C, 200 °C, 210 °C) were used to manufacture PLA samples with ten different extrusion rates or flow rates (ranging from 70% to 160%). Five samples of each configuration were manufactured and tested as per British and International standards. The combination of

simulation and experimental results was used to train the machine learning algorithms (Section 4.4) to predict the performance of the FFF-printed parts using the digital twin's output based on the testing results of the manufactured parts. In totality, the digital twin presented in this work is capable of asset management as per the simulation results and product performance predictions due to the use of machine learning algorithms.

3.1. PID/PWM Control Circuit Simulation

The extruder of the Anet® ET4 Pro 3D printer is controlled with a 12 V DC PID/PWM controller. The circuit maintains the user specified temperature of the extruder head (200 °C is the recommended temperature for PLA) measured via a K-type thermocouple attached next to the ceramic cartridge heater. For the 3D printer, the control circuit is a closed PID/PWM feedback loop with the user temperature as the input and the mean surface temperature on the extruder heating block as the output. The circuit also features two gains to adjust the values of the feedback signal from the K-type thermocouple and the PWM output signal into the 3D printer. For the simulation in ANSYS Twin Builder, the PID/PWM ECM was recreated as per Equation (1) [50] with an output range between 0 and 1 and the user's specified temperature as the input.

$$C(s) = K_p + \frac{K_i}{s} + K_d s = K_p(1 + \frac{1}{T_i s} + T_d s) \quad (1)$$

To adjust the reactions of the PID controller to setpoint changes and unmeasured disturbances (e.g., minimizing the variability of control error), the Ziegler Nichols second method algorithm was used to tune the PID and adjust the gain values [50]. Afterwards, PWM was used to transform the analogue PID output into a rectangular wave as per Equation (2) [51], with D being the duty cycle.

$$C(s) = D.C_{max} + (1 - D)C_{min} \quad (2)$$

The PWM signal is adjusted to simulate the heat flux generated by the 40 W ceramic heater. Finally, the average surface temperature of the heat block from the conjugate heat transfer is adjusted with feedback gain for the PID controller to complete the control circuit.

3.2. Extruder Assembly Simulation

The extruder assembly comprises the support plate, extruder, fan, and fan cover (Figure 1c). As the temperature is set at 200 °C for PLA, the ceramic heater gradually heats the aluminium block, which then transfers the heat through conduction to the extruder containing PLA. The fan performs an important function and prevents heat from creeping up the extruder and causing the filament to melt prematurely. For simulations, it is important to identify the heat transfer model that best describes the current conditions. The heat transfer and fluid flow in the extruder assembly (Figure 1c) prior to the melting of the filament is conjugate convective heat transfer with forced convection due to the presence of the fan [52]. The filament melting is a multiphase phenomenon with three phases (air, solid filament material, and melted filament material), while the melted filament is a non-Newtonian fluid that goes through the 0.4 mm microchannel at the end of the nozzle for deposition.

Due to the complexity and the different numerical modelling techniques required to simulate each one of the described systems (conjugate convective heat transfer simulation, multiphase melting simulation, and the microchannel non-Newtonian flow simulation), the numerical model of the entire extruder assembly is divided into three separate simulations with a coupled temperature boundary condition [53]. The coupled boundary transfers the temperature values among the simulations to ensure the physics simulated in the entire system is accurate, realistic, and consistent. Schematics of the coupled simulations are shown in Figure 5. The highlighted red areas in Figure 5 represent the coupled temperature boundary for the three systems. The computational domain for each simulation was

modelled according to the dimensions of the extruder assembly. For the conjugate heat transfer model, the ambient air domain was modelled with a uniform rectangular enclosure and zero-gauge pressure for the inlet as well as the outlet. The material melting domain is the filament cavity inside the extruder assembly alongside an extended air domain to model the melted filament deposition from the extruder nozzle. The extended air domain has zero-gauge pressure on all boundaries. Finally, a cylindrical domain was used in the microchannel simulation with the input as the mass flow rate computed from the filament melting simulation and the output as zero-gauge pressure. All domains were meshed in ANSYS Workbench using nonuniform tetrahedral elements with boundary layers for the internal and external flow regimes. The mesh element size was adjusted to ensure a 3% maximum temperature profile variation between runs for all simulations.

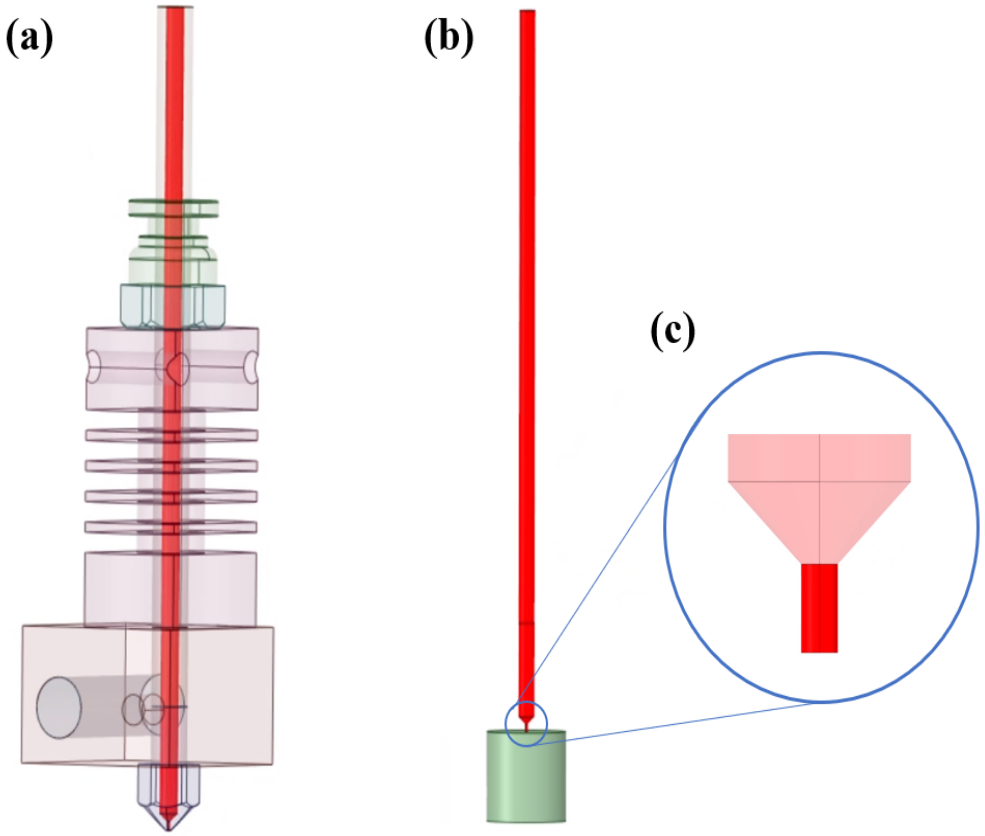


Figure 5. Shared filament temperature boundary among the FMUs of the digital twin: (**a**) Boundary in the forced convection simulation; (**b**) Boundary in the melting simulation; (**c**) Boundary in the microchannel simulation.

3.2.1. Conjugate Convective Heat Transfer Simulation

The numerical modelling for the extruder assembly encompassing multiple heat transfer and fluid flow starts with the forced convection simulation (due to the presence of the fan). All the extruder parts (Figure 1d) are modelled as solids, with their respective materials detailed in Table 3. The air is modelled as a 100 × 100 mm cubic enclosure surrounding the entire extruder assembly with zero-gauge pressure on all sides to model the ambient air for forced convection. Subsequently, the fan is modelled with a 3D fan zone [54,55] and the filament is modelled with a temperature coupling boundary. The fluid and solid material properties for the simulations were taken from the literature [56]. The coupled PRESTO pressure-based solver with first order implicit time formulation was utilized [57].

Table 3. Material properties for extruder components.

Components	Material	Properties		
		Density [kg/m^3]	Specific Heat Capacity [kJ/kg.K]	Thermal Conductivity [W/m.K]
Heating block & heat sink	Aluminium	2719	871	202.4
Nozzle	Brass	8390	380	123
Heat sink nut	Stainless steel	8030	502.43	16.27

The equations for continuity, momentum, and heat transfer have been solved using ANSYS Fluent software as shown below [58]:

$$\rho \frac{\partial u_i}{\partial x_i} = 0 \tag{3}$$

$$\rho \frac{\partial u_i}{\partial t} + \rho \frac{\partial}{\partial x_i}(u_i u_j) = -\frac{\partial P}{\partial x_i} + \frac{\partial \tau_{ij}}{\partial x_i} + \rho g \tag{4}$$

$$\tau_{ij} = \mu \left(\frac{\partial u_i}{\partial x_j} + \frac{\partial u_j}{\partial x_i} \right) - \frac{2}{3} \left(\frac{\partial u_k}{\partial x_k} \delta_{ij} \right) \tag{5}$$

$$\rho c \frac{\partial T}{\partial t} + \rho c \frac{\partial}{\partial x_i}(u_i T) = -P \frac{\partial u_i}{\partial x_i} + \lambda \frac{\partial^2 T}{\partial x_i^2} + \tau_{ij} \frac{\partial u_i}{\partial x_i} \ (fluid\ domains) \tag{6}$$

$$\rho c \frac{\partial T}{\partial t} = \lambda \frac{\partial^2 T}{\partial x_i^2} + q \ (solid\ domains) \tag{7}$$

For the forced convection simulation, based on the inlet values for the fan airflow, Reynolds number is in the turbulent range (3000–12,000); therefore, the *k*-ε turbulence model has been used for the fluid flow and the heat transfer phenomenon. The turbulent kinetic energy k and the dissipation rate ω are obtained from the following equations [59]:

$$\frac{\partial(\rho k)}{\partial t} + \frac{\partial(\rho u_j k)}{\partial x_j} = \rho P - \rho \varepsilon k + \frac{\partial}{\partial x_j} \left[\left(\mu + \frac{\mu_t}{\sigma_k} + \frac{\partial u_j}{\partial x_i} \right) \frac{\partial k}{\partial x_j} \right] \tag{8}$$

where $u_t = \rho C_\mu \frac{k}{\varepsilon}$ and the production terms P is defined as

$$P = v_t \left[\frac{\partial u_i}{\partial x_j} + \frac{\partial u_j}{\partial x_i} - \frac{2}{3} \frac{\partial u_m}{\partial x_m} \delta_{ij} \right] \frac{\partial u_i}{\partial x_j} - \frac{2}{3} k \frac{\partial u_m}{\partial x_m} \tag{9}$$

The specific dissipation rate of turbulent kinetic energy:

$$\frac{\partial(\rho \varepsilon)}{\partial t} + \frac{\partial(\rho u_j \varepsilon)}{\partial x_j} = C_{\varepsilon 1} \rho P \varepsilon - C_{\varepsilon 2} \rho P \varepsilon^2 + \frac{\partial}{\partial x_j} \left[\left(\mu + \frac{\mu_t}{\sigma_\varepsilon} \right) \frac{\partial \varepsilon}{\partial x_j} \right] \tag{10}$$

The coefficients for Equation (10) are shown in Table 4.

Table 4. Co-efficient values for *k*-ε turbulence model.

$C_{\varepsilon 1}$	$C_{\varepsilon 2}$	C_μ	σ_k	σ_ε
1.44	1.92	0.09	1	1.3

To reduce the complexity of the forced convection simulation, the axial fan is modelled using 3D fan zone element [54]. These are fluid cell zones that simulate the effect of an

axial fan by applying a distributed momentum source in a toroid-shaped fluid volume (i.e., a blade-swept volume). They offer several notable advantages such as calculation of swirl and radial velocities as well as providing comparable results to moving reference frame simulations and do not require the modelling of 3D rotating fan blade geometries, thus saving computation time and resources [60].

The following equations are used in the 3D fan zone for the momentum sources in the axial, tangential, and radial directions, which mimic the effect of the fan on the fluid [54]. The tangential momentum source is based on a turbomachinery relation, whereas the radial momentum source is based on a centrifugal force balance.

Axial:

$$S_a = \Delta P(Q)/h \tag{11}$$

Tangential:

$$S_t = \begin{cases} \frac{2W_{fan}r}{c_1|\Omega_{operating}|} & for\ R_h < r \leq R_{ip} \\ \frac{2W_{fan}R_{ip}^2}{c_1 r|\Omega_{operating}|} & for\ R_{ip} < r < R_t \end{cases} \tag{12}$$

Radial:

$$S_r = \frac{\rho V_\Phi^2}{r} \tag{13}$$

Table 5 gives the values for 3D fan zone parameters.

Table 5. Values for 3D fan zone parameters.

R_h	R_t	h	R_{ip}	$\Omega_{operation}$	$\Delta P(Q)$
5 cm	2 cm	1 cm	2.5 cm	2000 rpm	20 mmHg

3.2.2. Material Melting Simulation

The melting simulation focuses on the transient phase change in the PLA filament. The melting is modelled with the enthalpy-porosity method [61], which separates the melting material into three phases, including solid, liquid, and a porous mushy zone. The mushy zone has a porosity coefficient from zero (for complete solid) to one (for complete liquid). Furthermore, the range is determined based on the solidus temperature and liquidous temperature of the material. When the PLA filament enters the mushy zone and the subsequent liquid zone, the viscosity model is set to the cross Williams–Landel–Ferry (WLF) non-Newtonian viscosity fluid model [62]. Additionally, the PLA melting domain features an extended air zone to accurately capture the melted filament flow rate as it is deposited through the nozzle. The filament feed rate is modelled with a constant mesh velocity on the domain inlet [63].

For numerical discretization, a second-order upwind scheme for the momentum, energy, turbulence, and VOF (volume of fluid) equations as well as a least square-cell based system for calculating the gradient of scalar variables was used [64]. The height-based layering dynamic mesh technique was used to model the filament feed rate with a constant speed of 8mm/s (Table 1). The interface between the air and the PLA creates a multiphase phenomenon with three phases (air, solid filament material, and melted filament material). For the multiphase simulation, the effective fluid properties on the boundary cells were computed as the volume weighted average of the present phases. The PLIC (Piecewise Linear Interface Construction) scheme was used to determine the phase interfaces on the border cells [65].

The filament melting simulation is solved by using the enthalpy-porosity model [61]. The enthalpy of the material in combination with a pseudo porous zone is utilized to

indicate the transition of the filament from solid to liquid. The energy equation for melting is written as follows [61]:

$$\rho\frac{\partial H}{\partial t}+\rho\frac{\partial}{\partial x_i}(u_iH)=\lambda\frac{\partial^2 T}{\partial x_i^2}\ ,\ H=h_{ref}+\int_{T_{ref}}^{T}CdT+\beta L \tag{14}$$

The liquid fraction is defined as

$$\beta=\begin{cases}0\ if\ T<T_s\\ \frac{T-T_s}{T_l-T_s}\ if\ T_s<T<T_l\\ 1\ if\ T>T_l\end{cases}\ ,\ A(\beta)=\frac{A_{mush}(1-\beta)^2}{\beta^3+\epsilon} \tag{15}$$

Additionally, a sink term in the form of $S=-A(\beta)u_i$ is added to the momentum equation to account for the presence of the solid material in the domain. Table 6 shows the material properties of the PLA used in the current study [56].

Table 6. Properties of PLA material.

#	Properties	Values
1	Solid density (gr/cm^3)	1.252
2	Liquid density (gr/cm^3)	1.073
3	Specific heat at 55°C (J/kg°C)	1590
4	Specific heat at 100 °C (J/kg°C)	1955
5	Specific heat at 190 °C (J/kg°C)	2060
6	Thermal conductivity at 48 °C (W/m°C)	0.111
7	Thermal conductivity at 109 °C (W/m°C)	0.197
8	Thermal conductivity at 190 °C (W/m°C)	0.195
9	Liquidus temperature (°C)	191
10	Solidus temperature (°C)	165
11	Glass transition temperature (°C)	65
12	Latent heat of fusion (J/g)	93

The viscosity model used for the filament in the melting simulation is the non-Newtonian cross-WLF model. This model describes the pressure, temperature, and shear rate dependencies of viscosity using the following equation:

$$\eta=\frac{\eta_0}{1+\left(\frac{\eta_0\dot{\gamma}}{\tau^*}\right)^{1-n}}\ ,\ \eta_0=D_1e^{-\frac{A_1(T-T^*)}{A_2+(T-T^*)}}\ ,\ T^*=D_2+D_3P \tag{16}$$

The co-efficient values in Equation (16) are given in Table 7.

Table 7. Co-efficient values for the cross-WLF model.

n	τ^*	D_1	D_2	D_3	A_1	A_2
0.25	1.00861×10^5	3.31719×10^9	373	0	20.2	51.6

The interactions among the phases (air, solid filament, and melted filament) present in the second simulation are modelled using the volume of fluid (VOF) method [65]. The VOF model solves for the volume fraction α in a multiphase system with N secondary phases

plus one primary phase where the sum of all the volume fractions is equal to one as given by the following equation:

$$\frac{\partial}{\partial t}(\rho_n \alpha_n) + \frac{\partial}{\partial x_i}(\rho_n \alpha_n u_{ni}) = S_n \, , \, \sum_{n=1}^{N} \alpha_n = 1 \tag{17}$$

3.2.3. Microchannel Simulation

After the phase change process, the melted filament is extruded through a 0.4 mm diameter channel inside the end nozzle. This diameter classifies the fluid inside as a microchannel with non-Newtonian rheology. The flow regime is indicated by the Reynolds number of the fluid. Since the melted PLA follows a cross-WLF model, the fluid viscosity is dependent on the shear rate at different diameters. This is varied between 6×10^3 and 6×10^4 Pa.s, and, with the constant feed rate of the printer, the Reynolds number is in the order of 10^{-4} to 10^{-5}, which makes the flow regime laminar with a low Reynolds number [66]. In a low Reynolds number flow regime, the Navier-Stokes equations could be simplified to be time independent. However, since the previous simulations and the control model are all time dependent, the microchannel simulation is also modelled using the time dependent Navier-Stokes equation described in Section 3.2.1 (Equations (3)–(6)). The microchannel flow in the nozzle is modelled with the same enthalpy-porosity melted filament domain discussed in Section 3.2.2 (Equations (14) and (15)) to capture the velocity, temperature, and liquid fraction boundary layer profiles. The inlet mass flow and temperature are calculated from the melting simulation mass flow rate, and the nozzle wall temperature profile is taken from the coupled temperature boundary.

3.3. Experimental Validations and Testing

To ensure the reliability of the extruder assembly simulations and control circuit from the digital twin, their results must be validated against experimental data gathered from the Anet® ET4 Pro 3D printer while manufacturing a PLA dog-bone sample. The first element is the PID/PWM controller circuit, and its role is to maintain the user specified temperature of 200 °C (operating temperature of PLA) to manufacture the dog-bone sample. To validate the simulations for the PID/PWM control circuit, the PWM output going to the ceramic heater from the 3D printer controller was captured using a LeCroy waveRunner 204Xi 2 GHz oscilloscope (Test Equipment Solutions, Reading, UK) [67]. A FLIR C5 thermal imaging camera (Teledyne FLIR, Kent, UK) [68] was used to capture the temperature distribution of the extruder assembly to validate the conjugate convective heat transfer simulation. Furthermore, the heating block's temperature was monitored using two additional K-type thermocouples (operating range of −100 °C to +500 °C) connected to an external data logger Datataker DT80 (Omni Instruments, UK) [69]. The measurements were taken for 2.5 min as the heater started from room temperature, reached 200 °C, and maintained the 200 °C temperature effectively. These thermocouples were fixed to the heating block of the 3D printer using heat resistant Kapton tape. Figure 6 shows their position on the heating block. The thermocouple measurements were used to validate the temperature values obtained from the conjugate convective heat transfer simulation.

Furthermore, the mass flow rate of the 3D printer based on the user specified deposition speed of 50 mm/s (Table 1) was calculated using the deposited PLA's dimensions and flow rate percentage according to Equation (18) [70]. It was also measured experimentally by printing a hollow single layer thickness square sample and measuring its mass. This measurement provided the average mass flow rate of the PLA, which was used to validate the mass flow rate of the simulation to ensure realistic results.

$$\dot{m} = \rho \times D_s \left(h(w \times inf_r - h) + \pi \left(\frac{h}{2} \right)^2 \right) \tag{18}$$

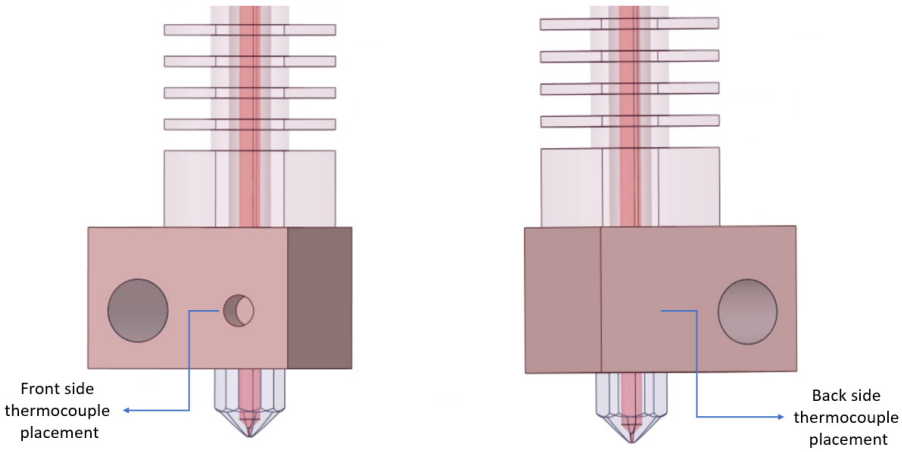


Figure 6. Placement of the external thermocouples for validating the temperature profile of the forced convection simulation.

After validating the simulations, a variety of dog-bone PLA parts were printed at four different temperatures (180 °C, 190 °C, 200 °C, 210 °C) and ten different extrusion rates (ranging from 70% to 160% in 10% increments). These are the two input variables that were modified, whereas all the other parameters were kept constant as shown in Table 1. From these samples, the surface roughness, hardness, and fracture loads (for tensile strength) were measured. Five samples of each configuration were manufactured and tested. For the surface roughness analysis, Surftest SJ-210 (Mitutoyo, Andover, UK) contact-type surface profilometer with a detector measuring force of 0.75 mN and a range of 360 µm [71] was used. The traverse direction was diagonal to the building direction at an angle of 45°, as per ISO 21920-2:2021 [72]. Three measurements were taken on each sample with a measuring speed of 0.5 mm/s. After the surface roughness analysis, the samples were subjected to indentation hardness testing as per BS EN ISO 868:2003 [73] using a Shore D durometer. The indentation was measured at five different points to obtain an average hardness value for all the samples. Tensile testing was conducted as per BS EN ISO 527-2:2012 [47] using a Tinius Olsen Universal Tensile Testing Machine at a crosshead speed of 1.5mm/s according to the standard. These experimental results are required along with the simulation data to develop a database to be used for training and validating the machine learning algorithms.

3.4. Reduced Order Modelling

It is to be noted that creating the simulation data for all the different combinations of extrusion temperatures and extrusion rates is time-consuming. Therefore, to generate these results in a timely and resource efficient manner, a reduced order model (ROM) has been utilised. The ROM can provide the required simulation data significantly faster compared to the digital twin. To reduce the time and computation resources needed to digitally print each sample, only 50% of the samples were simulated using the digital twin, and the rest of the temperature distributions were obtained by developing a reduced order model.

ANSYS utilizes a family of model order reduction techniques known as the reduced basis approach or reduced order modelling by projection. A summarized description of the methodology is as follows [74]. Assuming a system of linear equations in the form of $K(\mu)u = F$, there exists a set of basis functions Φ which satisfy the following equation:

$$\Phi^T K(\mu)\Phi\alpha = \Phi^T F \tag{19}$$

This projection forms the stiffness matrix variable subspace into the much smaller basis subspace (also known as snapshots) and is referred to as the POD-Galerkin projection.

After selecting the proper basis function form for the problem, the residual error of the model order reduction can be calculated using the following equation:

$$err^2 = \frac{\| K(\mu)\Phi\alpha - F \|^2}{\| F \|^2} \tag{20}$$

Some notable examples of basis functions are the Craig-Bampton model [75], the Krylof model [76], etc. ANSYS uses the Krylof model in the ROM Builder, and it is used to create the reduced order model in this study. The output from the ROM is used to generate the database required for the machine learning algorithms.

3.5. Machine Learning Development

The machine learning algorithms will use the final temperature distribution of the melted filament inside the microchannel to predict the performance of the parts, indicating that a replica of the physical part must be simulated for each sample individually. As discussed previously, the performance of the printed parts is directly related to the properties of the filament coming out of the nozzle. Therefore, predicting the performance of the parts using the digital twin is dependent on the information available in the final nozzle simulation, such as the filament flow rate, output temperature, temperature boundary layer, and liquid fraction. To connect the mesh grid data to tangible user-friendly information, convolutional neural network and random forest classifier were used to predict the printed part performance from the simulation data [77,78]. Both algorithms need an existing database to train their respective networks. An extensive collection of printed PLA parts and their respective experimental data is required by the database. The corresponding nozzle simulations were carried out using a Reduced Order Model approach to save time and resources (Section 3.4).

3.5.1. Convolutional Neural Network

The basis of the convolutional neural network is a combination of weighted neurons using the following equation [79]:

$$\hat{P}_i = \Lambda(\sum_{j=1}^{J} w_j P_j) \tag{21}$$

where $\hat{P}_i = \{\hat{P}_1, \hat{P}_2, \ldots, \hat{P}_N\}$ is the N neuron output layer relative to the previous $\{P_1, P_2, \ldots, P_j\}$ input layer, w_j is the weights and biases denoted to the P_j neuron, and $\Lambda(\sim)$ is the ReLU (rectified linear unit) neuron activation function used in this study. The weights and biases are determined using the Adam stochastic optimization method for the categorical cross entropy loss function. The loss function is as follows:

$$Loss = -\sum_{i=1}^{n} y_i \log \hat{y}_i \tag{22}$$

where $\hat{y}_i$ is the $i'th$ performance class in the model output, with y_i being the corresponding target value. The adam optimizer minimizes the loss function's value using an iterative gradient descent methodology. The equations are as follows:

$$w_t = w_{t-1} - \eta \frac{\hat{m}_t}{\sqrt{\hat{v}_t} + \varepsilon} \tag{23}$$

$$\hat{m}_t = \frac{\beta_1 m_{t-1} + (1 - \beta_1) g_t}{1 - \beta_1^t} \tag{24}$$

$$\hat{v}_t = \frac{\beta_2 v_{t-1} + (1 - \beta_2) g_t^2}{1 - \beta_2^t} \tag{25}$$

$\hat{m}_t$ and $\hat{v}_t$ are bias corrected moving averages of the loss function gradient. Lastly, the output layer is Softmax activated to determine the sample's final class. The equation is as follows:

$$Softmax(y_i) = \frac{e^{y_i}}{\sum_{k=1}^{n} y_k} \tag{26}$$

The current study utilizes four hidden layers with 60 to 40 neurons [80]. The final output layer is separated into 3 performance classes (good, average, and bad).

3.5.2. Random Forest Classifier

Random forest is an ensemble learning algorithm that constructs a multitude of uncorrelated regression trees. Each regression tree requires a splitting and stopping criterion which is determined based on the following equation [81]:

$$\min_{j,s}\left[\min_{c1}\sum_{x_i\in R_1(j,s)}(y_i-c1)^2+\min_{c2}\sum_{x_i\in R_2(j,s)}(y_i-c2)^2\right] \tag{27}$$

where s is the stopping point and $j = 1, 2, 3, \ldots, p$ is the splitting point for the p possible splitting variables. For every target value of y_i of the sample x_i, the best split between the $R_1(j,s) = \{x|x_j \leq s\}$ and $R_2(j,s) = \{x|x_j \geq s\}$ is determined by minimizing the loss of each target value minus the average of the target values that fall into that region $c_{1,2} = ave(y_i|x_i \in R_{1,2}(j,s))$. This process of splitting the parent node into two child nodes is repeated until the stopping criterion is reached. The current study utilizes 50 trees [81].

4. Results and Discussion

4.1. PID/PWM Control Circuit Simulation and Validation

The purpose of the digital twin is to reproduce the conditions of the physical asset accurately; therefore, the PID/PWM output signal must have a comparable timing and duty cycle. In other words, since the geometry, heat rate, and heat loss are the same as for the physical extruder assembly, the PID/PWM output duty cycle of the digital twin and the Anet® ET4 Pro 3D printer control circuit must be comparable.

The role of the PID/PWM within the 3D printer is to maintain the user specified temperature by switching the ceramic heater on and off with a certain duty cycle (based on the heating block's temperature and the PID feedback loop). The temperature difference between the block and the user setting goes into the PID. If the temperature of the block is (say) 202 °C and the user setting is 200 °C, then the heater must turn off to decrease the temperature, indicating that the duty cycle is lower, and vice versa. In the digital twin's controller, the PWM module transforms the PID duty cycle output to a rectangular waveform suitable for the FMUs corresponding UDFs (user defined functions). To validate this scenario, a PLA dog-bone sample was printed at 200 °C with 8 mm/s feed rate and 50 mm/s deposition speed (Table 1). The printer volume flow rate was measured during the printing process at 1018.24 mm^3/s and subsequently the mass flow rate, using the PLA density from Table 6, was calculated as 13.949×10^{-6} kg/s as per Equation (18). The printing temperature was monitored at both sides of the heating block as shown in Figure 6. The oscilloscope measurement of the PWM output signal is shown in Figure 7. The red line in Figure 7 represents a rising edge (transitioning from OFF to ON or 0 to 12 V). Points A to C denote the 3D printer going from room temperature to 200 °C. From B to C, the PID/PWM controller is switching the heater ON and OFF to maintain the 200 °C, hence the significant number of red lines.

The section denoted in Figure 7 as DE has been enhanced to show the 10 s interval of the PID/PWM waveform and compared to the digital twin's output in Figure 8. It is evident that both the PID/PWM circuits (digital twin and physical) are controlling similar systems due to matching time intervals for the ON and OFF sections of the square waveform. This implies that, in both cases, the duty cycle for the ceramic heater turning ON and OFF while maintaining a 200 °C temperature has approximately the same time interval, indicating

that the heater takes the same amount of time in heating the block and staying OFF for the block to cool down.

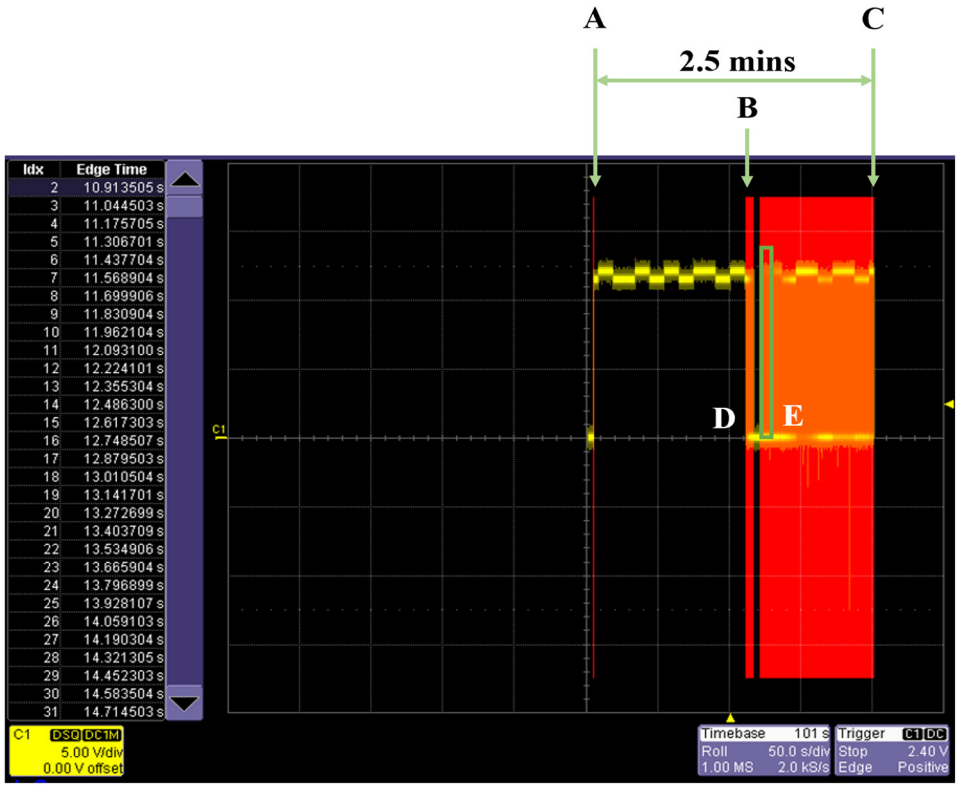


Figure 7. Oscilloscope output of the PWM waveform, A to C is the measurement runtime at 2.5 min while point B marks the start of pulse modulation and section D to E is where the PID/PWM simulation is validated.

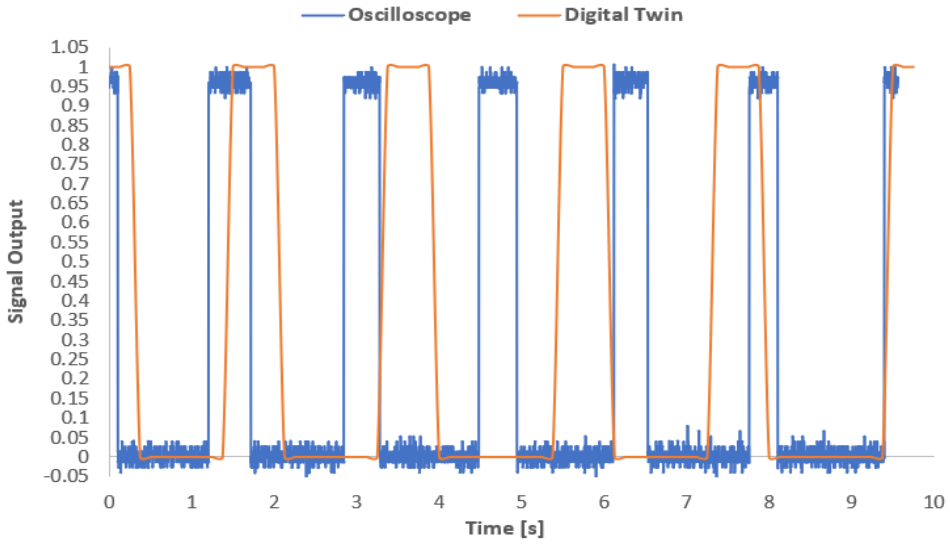


Figure 8. Validation of the PWM signal.

4.2. Extruder Assembly Simulation and Validation

After applying the PID/PWM control to the extruder assembly simulations, an in-depth analysis of the filament melting process can be undertaken. As described in Section 3.2, the numerical model of the entire extruder assembly is divided into three separate simulations with a coupled temperature boundary condition. These simulations and their subsequent validations are described below.

4.2.1. Conjugate Convective Heat Transfer Simulation and Validation

This simulation aims to discern how much heat is transferred to the PLA inside the extruder from the time the printing process begins at room temperature to reach the PLA's operating temperature. The internal and external heat transfer of the extruder assembly needs to be modelled due to the presence of a heat source (ceramic heating element) and the heat loss due to the fan cooling the extruder. This will help in observing the temperature profile of the system due to heat generation and heat loss. Furthermore, the control circuit of the PID/PWM helps the extruder assembly in maintaining a constant temperature on the heating block to print a PLA sample at 200 °C. This conjugate convective heat transfer simulation controlled by the PID/PWM circuit (Section 4.1) is shown in Figure 9, highlighting the temperature distribution and the air flow streamlines around the extruder assembly.

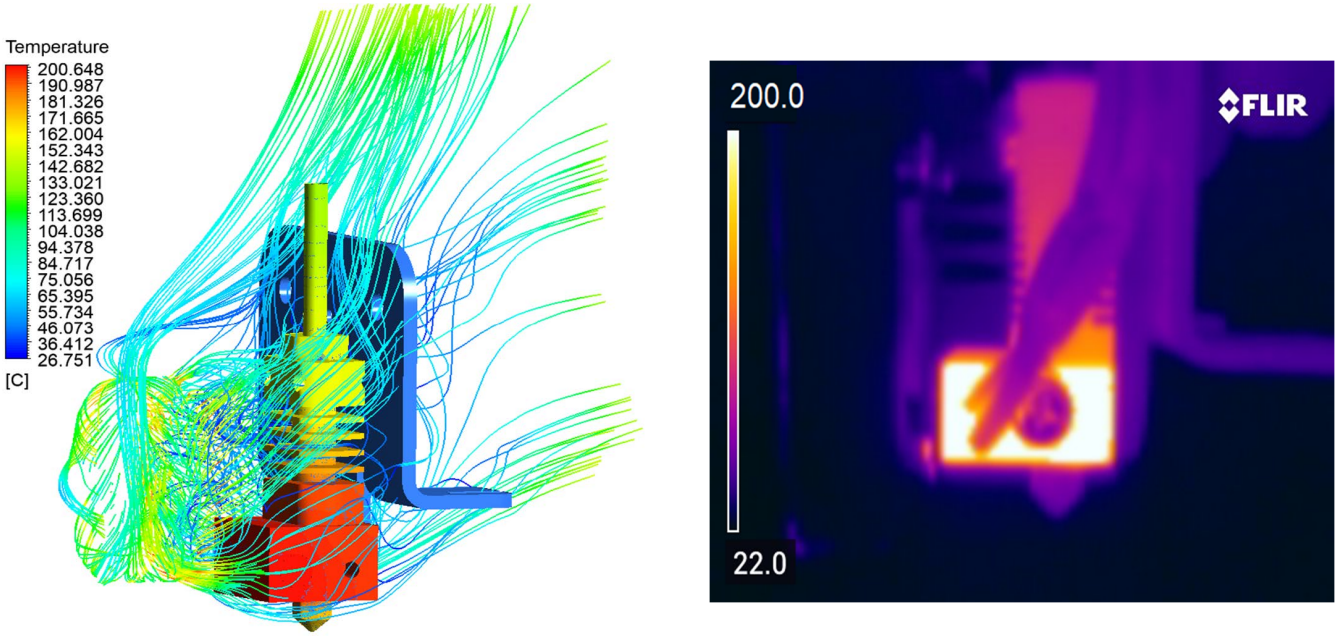


Figure 9. Simulation and experimental results for convective heat transfer. Left is the forced convection simulation with both temperature contours and airflow streamlines around the extruder. Right is the thermal imaging camera result of the same extruder while printing.

The simulation in Figure 9 shows that that the heating block maintains a constant temperature of 200 °C, whereas the rest of the system shows a temperature below the PLA's liquidous temperature to avoid premature melting. This has been achieved by the air flow generated by the fan as observed by the air streamlines around the extruder assembly. It is evident that majority of the air flow is around the heat sink, as its main purposes are to spread heat away from (cool down) the filament's path when it is outside of the melt zone and to avoid heat creep [82]. However, a portion of the air flow escapes under and around the heating block and the nozzle. This creates a small temperature drop around the edges of the heating block and at the end of the nozzle (approximately 5 to 12 °C at maximum). The minor temperature drop generates a temperature boundary layer in the 0.4 mm microchannel (inside the nozzle). The temperature boundary layer is dependent on the temperature as well as the material mass flow rate and influences the performance of the final product (Section 4.2.3).

In practice, the PLA starts the phase change at 150 °C–165 °C; therefore, the heatsink is designed to keep the feeding filament prior to the heating block lower than that temperature. On the other hand, the heating block must maintain a uniform temperature dictated by the user and the control system to ensure smooth filament deposition. These characteristics have been shown in Figure 9. To validate this temperature profile, a thermal image was

taken using the FLIR C5 thermal imaging camera that highlights the temperature rise from room temperature to 200 °C (Figure 9). Furthermore, it can also be observed from the simulation and the thermal image that the uniform temperature of the heating block is maintained at 200 °C, whereas the heat sink is maintaining a lower temperature (lower than the PLA's melting temperature).

After validating the temperature profile of the extruder assembly, the temperature values obtained from the front and back of the heating block within the simulation were compared with the values obtained from the two additional K-type thermocouples (Section 3.3; Figure 6). The comparisons in Figure 10 show a good agreement between the simulation and experimental results. They show similar characteristic curves and are closely aligned as they reach the constant temperature of 200 °C. The mean squared error is 3% for Figure 10a and 4.2% for Figure 10b, which is quite small, thus indicating a good agreement between the simulation and experimental results.

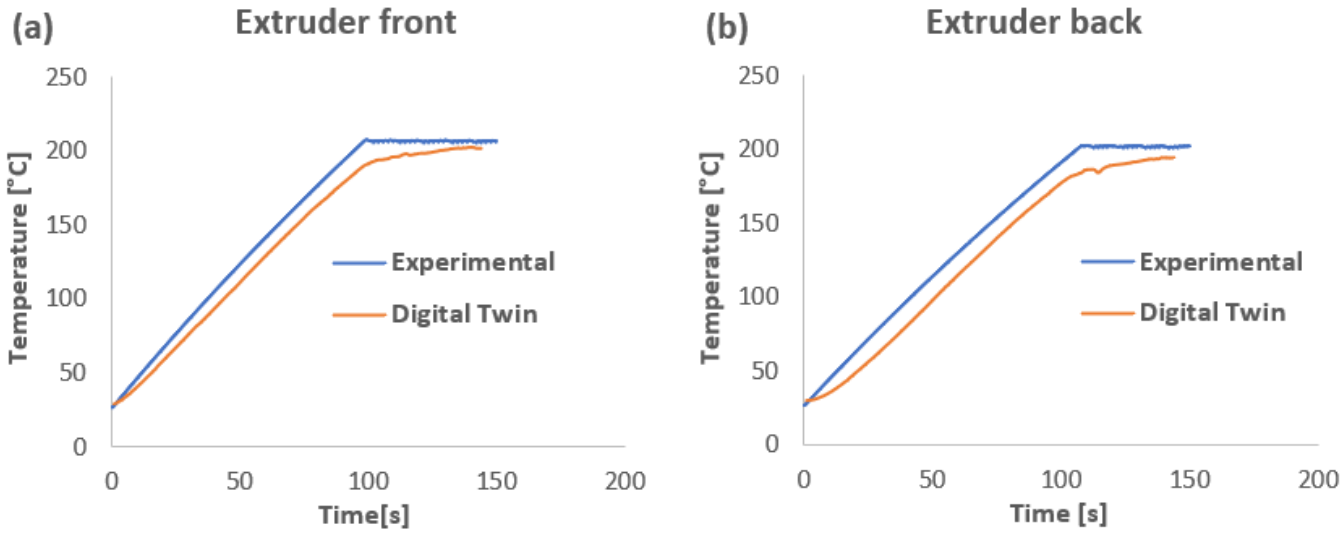


Figure 10. Comparison between experimental and digital twin simulation results: (**a**) Extruder front profile; (**b**) Extruder back profile.

4.2.2. Material Melting Simulation and Validation

The process of the filament melting is shown in Figure 11 with the temperature profile (Figure 11a) and liquid fraction (Figure 11b). The multiphase model depicts how the filament is melted and deposited onto the print bed as the 3D printer continuously feeds more material into the extruder assembly. Additionally, Figure 11 demonstrates that the liquid fraction of the melted PLA in the domain (Figure 11b) follows the same profile as the temperature distribution of the PLA inside the extruder (Figure 11a).

Figure 12 shows the volume fraction of the non-Newtonian melted PLA in the extruder nozzle, demonstrating the smooth deposition of the PLA material, and gives the average mass flow rate. This value is calculated as 13.00×10^{-6} kg/s as per Figure 13. The sustained deposition rate matches the experimental calculation of 13.949×10^{-6} kg/s as per Equation (18) (Section 3.3). This shows a difference of only 6.8% between the simulation and calculated values. To further highlight the details of the temperature and the liquid fraction boundary layers, the third simulation focuses specifically on the 0.4 mm diameter microchannel.

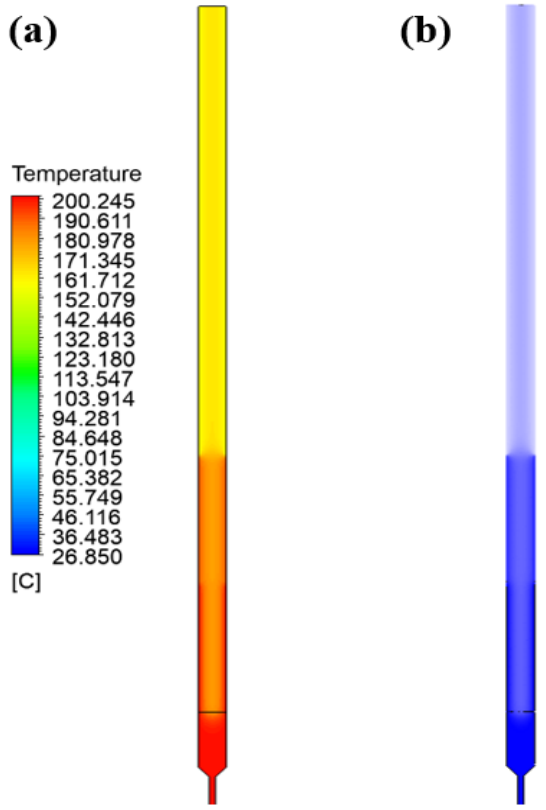


Figure 11. PLA inside the extruder assembly; (**a**) Temperature profile of PLA; (**b**) Liquid fraction of PLA.

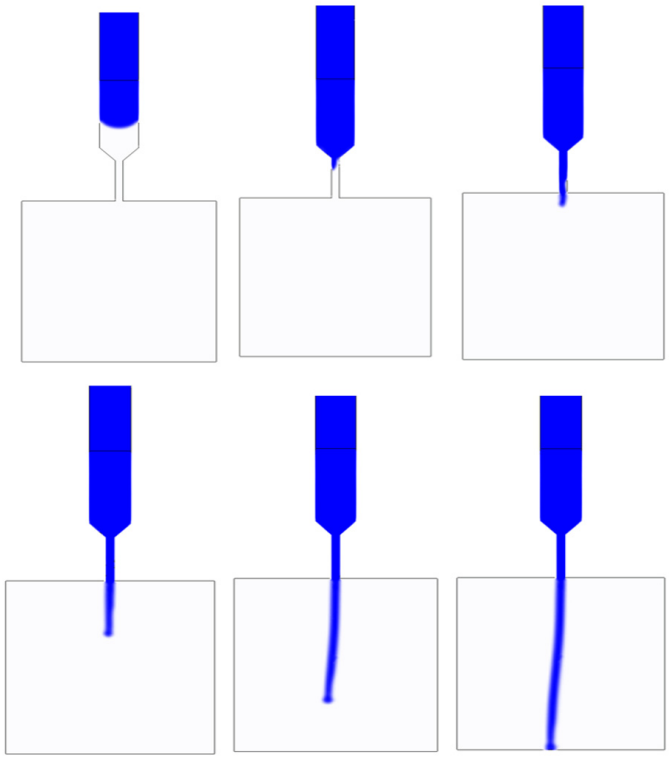


Figure 12. Time-lapse of the volume fraction of the melted PLA filament flowing through the nozzle.

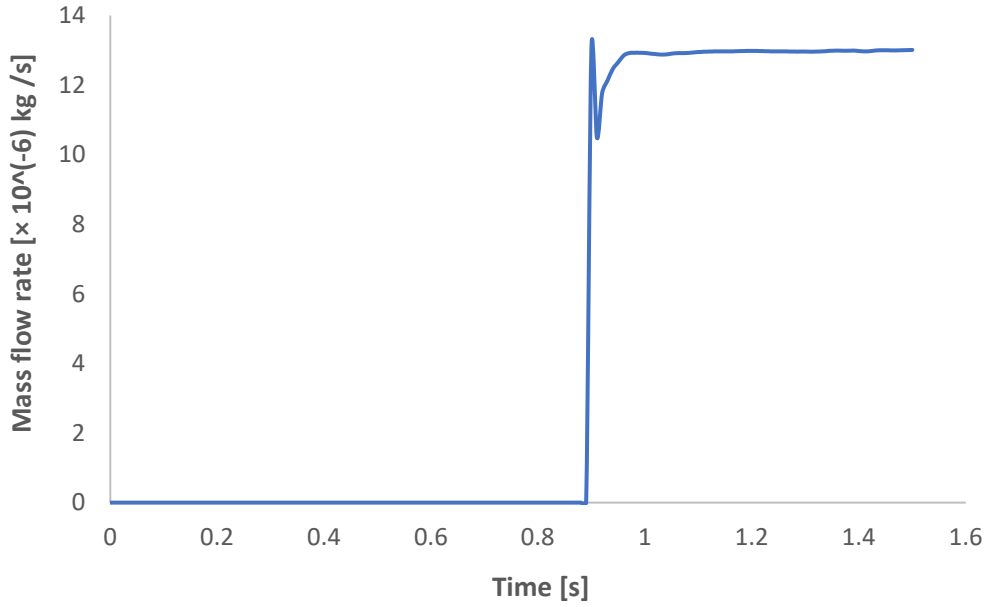


Figure 13. PLA mass flow rate from material melting simulation.

4.2.3. Material Flow though the Microchannel

The melted filament has a laminar flow regime through the nozzle. The small temperature difference between the beginning of the nozzle inside the heating block and the tip of the nozzle creates a temperature boundary layer inside the extruder nozzle. Under the correct printing conditions, the thickness of the boundary layer is negligible and has no effect on the performance of the printed parts. This has been demonstrated in Figure 14, as 200 °C is the optimal temperature for printing PLA and the length shown is 2 mm. It is also evident that the liquid fraction boundary layer is minimal and ensures a smooth flow of the material from the 0.4 mm diameter nozzle. However, utilizing composite filaments or out of bound printing conditions will result in undesirable part performance, clogging/jamming of the nozzle, or under and/or over extrusion [10,17]. Using the controlled simulations developed in the current study, the material output of the printer can be carefully tuned to the desired outcome prior to the physical printing process, thus saving considerable time, material, and energy.

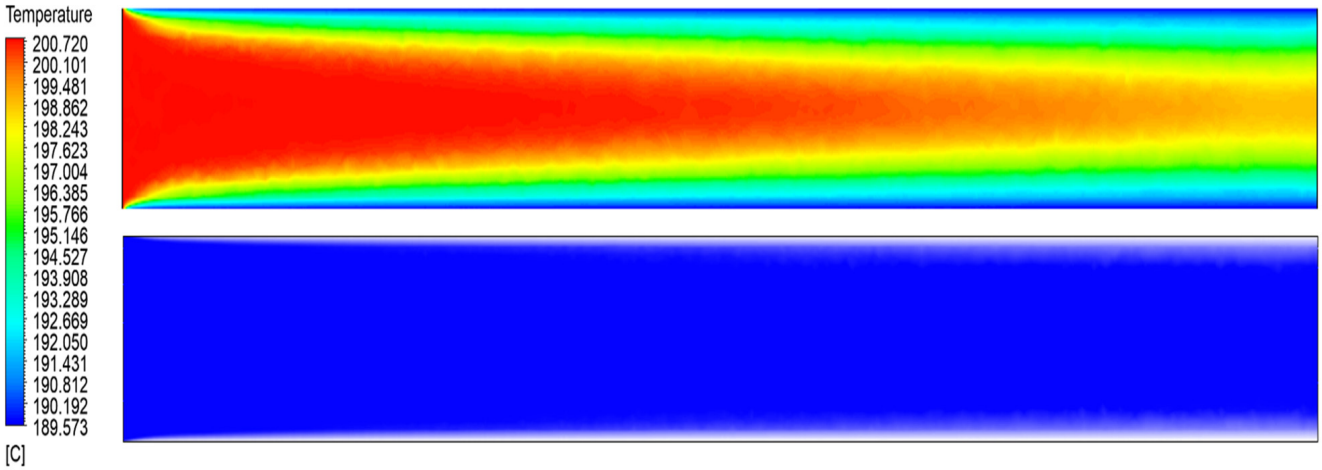


Figure 14. Temperature (**top**) and liquid fraction (**bottom**) contours of the melted filament going through the nozzle from the microchannel simulation.

Furthermore, the state of the filament inside the microchannel is the determining factor in the performance of the printed part. The filament mass flow rate and the temperature

distribution directly influence the part's surface roughness, hardness, and tensile strength. For example, a high mass flow rate will result in better tensile strength but a bad surface finish due to layer overlaps and a heavier part due to excess material (over extrusion). On the other hand, a partially melted filament could block the nozzle and produce a nonuniform part with unwanted gaps and holes (under extrusion), resulting in maintenance issues and the poor quality of the printed parts. However, these correlations are mostly qualitative observations and difficult to link to the quantitative output of the simulation for accurate and reliable predictions of how the extruder will operate and the performance of the final parts. Determining an analytical correlation between the physically tested parts and the digitally printed parts require a complete heat transfer analysis of all of the simulations to find the relation between dimensionless numbers such as Nusselt, Reynolds, and Prandtl with the experimental tests [83]. Alternatively, a machine learning tool can be used to classify the parts into categories and predict the results for the new parts based on the previous dataset [84], which is the approach used in the present study. This has been achieved with the help of reduced order modelling and machine learning algorithms (convolutional neural network and random forest) as discussed below.

4.3. ROM for Extrusion Temperature and Extrusion Rate

After successfully validating the controlled extruder assembly simulations and ensuring the measured outputs match the experimental data, a set of extruder temperature profiles and mass flow rate snapshots were captured from the digital twin to develop the ROM. The temperatures range from 180 °C to 210 °C in 10 °C increments. The extrusion rates range from 70% to 160% in 20% increments. This is being done because 50% of the data is required to develop the ROM and subsequently generate results for the remaining 50%.

The result of the final nozzle microchannel simulation for each scenario is used to create a ROM of the same simulation capable of instantly calculating the filament's characteristics. These characteristics (temperature, velocity, liquid fraction) within the ROM can be computed for any combination of input variables (e.g., nozzle wall temperature distribution, input mass flow rate, and temperature). Table 8 shows the ROM temperature profiles inside the microchannel of the nozzle at different extrusion temperatures and extrusion rates. As the extrusion temperature increase, the PLA melts quickly and can reduce the boundary layer. The same scenario takes place as the extrusion rate increases, as more material should be extruded out of the nozzle. However, it is difficult to visualise the decrease in the thickness of the boundary layer from the simulation results alone, as the difference among the different extrusion temperatures/rates is not visually evident and is quantitatively linked to the performance of the FFF-printed products. Therefore, the use of machine learning algorithms can help in evaluating these simulation results along with experimental data to provide useful insights for effective decision making. These ROM results will also help in developing a comprehensive database for the PLA material as per the input parameters (extruder temperature and extrusion rate). This database is used to train two separate machine learning algorithms to connect the temperature profile to the final part's performance. The performance can be affected due to changes in extruder temperature as well as extrusion rate, and this effect is explained further in Section 4.4.

Table 8. ROM results for nozzle microchannel temperature profiles.

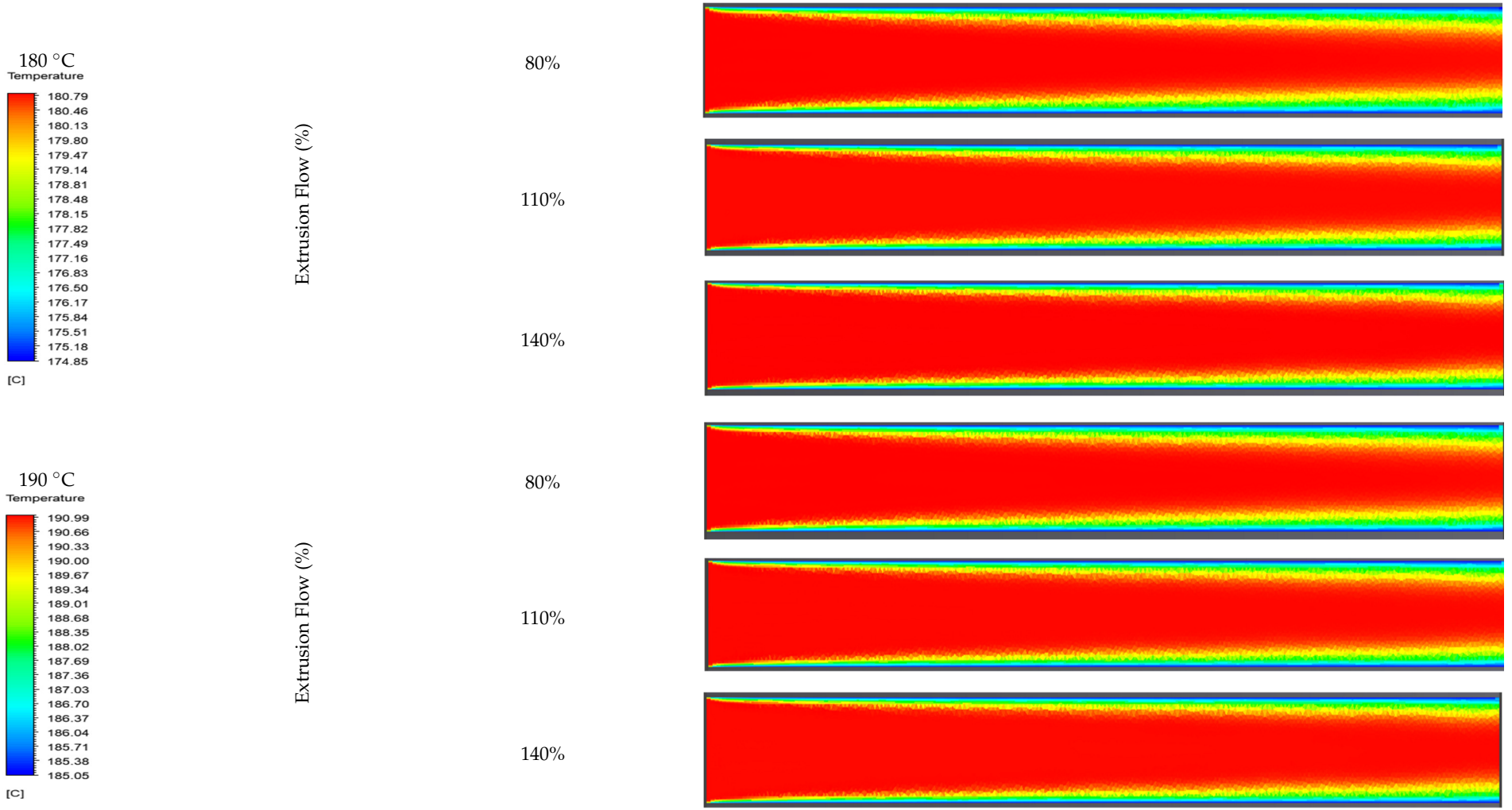
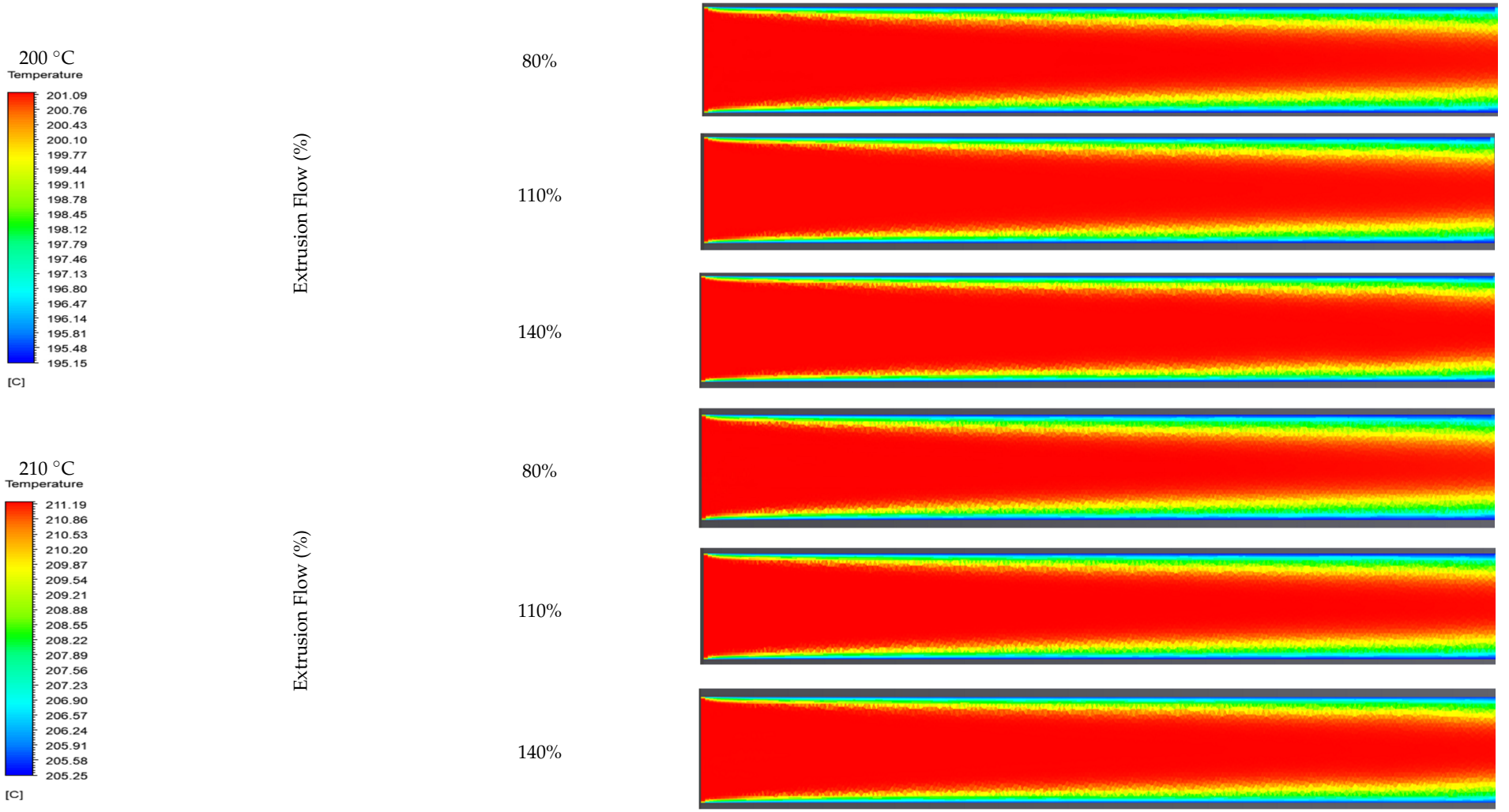


Table 8. *Cont.*


200 °C
Temperature
201.09
200.76
200.43
200.10
199.77
199.44
199.11
198.78
198.45
198.12
197.79
197.46
197.13
196.80
196.47
196.14
195.81
195.48
195.15
[C]
Extrusion Flow (%)
80%
110%
140%
210 °C
Temperature
211.19
210.86
210.53
210.20
209.87
209.54
209.21
208.88
208.55
208.22
207.89
207.56
207.23
206.90
206.57
206.24
205.91
205.58
205.25
[C]
Extrusion Flow (%)
80%
110%
140%

4.4. Implementation of Machine Learning for Performance Classification

The experimental results for the surface roughness, shore D hardness, and tensile strength of the experimental parts are shown in Figure 15. As can be seen in Figure 15a, the surface roughness values were higher for samples printed at lower extrusion rates (under extrusion) and smallest for samples printed at 90% and 100% extrusion rates, becoming higher again at higher extrusion rates (over extrusion). It is to be noted that samples printed at up to 120% extrusion rates have been presented, as the higher extrusion rate samples resulted in peak/valley measurements exceeding the 360 µm range of the Surftest SJ-210 contact-type surface profilometer [17]. This also means that there are fewer samples for the surface roughness compared to the hardness and tensile strength measurements. When the surface finish became poorer in the under and over extruded samples, the hardness values also lowered, and the highest values were observed at the 90% and 100% extrusion rates where the lowest surface roughness values were observed (Figure 15b). This is because there was proper layer contact at these extrusion rates, thus resulting in a higher resistance to indentation [10]. Figure 15c shows that, as the extrusion flow rate increased, the tensile strength also kept increasing until 150% flow, and then a sharp decline was observed for samples printed at a 160% flow rate. This is because the 160% flow rate samples had extremely rough surface finish due to excessive material, which led to stress risers on the surface, causing premature failure [17].

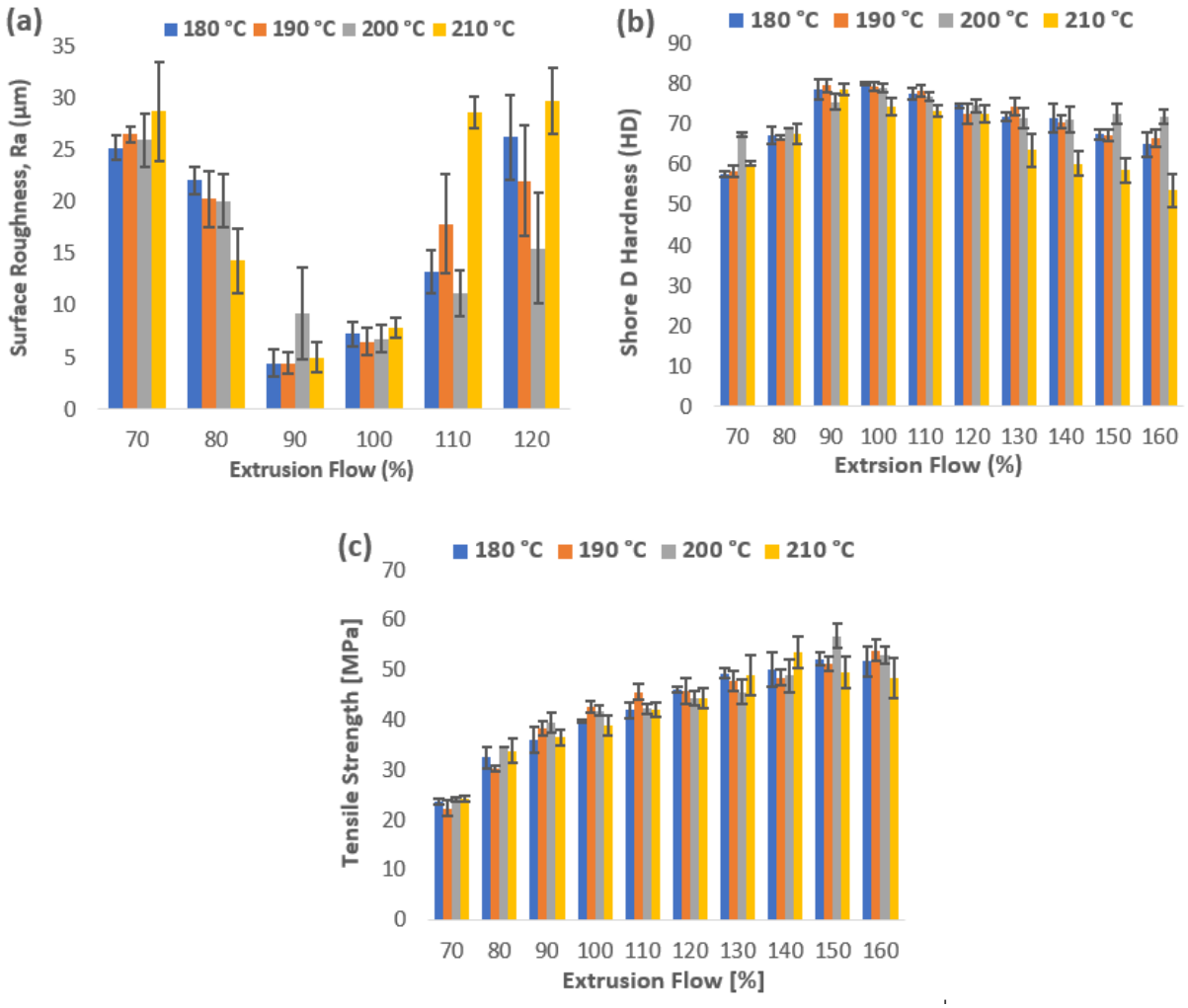


Figure 15. PLA experimental results; (**a**) Surface roughness; (**b**) Shore D hardness; (**c**) Tensile strength.

These experimental results (surface roughness, hardness, and tensile strength) have been used as the basis for defining a classification, i.e., good, bad, and average, as per

Table 9, and these categories are shown in Figure 16. The thresholds have been defined for a strong product to be used for load bearing applications. In such a case, higher tensile strength and hardness are essential to the performance of the product. However, good surface finish is not a high priority. These categories can help designers and manufacturers in choosing the right input parameters to achieve the desired results in terms of surface roughness, hardness, and tensile strength.

Table 9. Thresholds for categorization.

Parameters	Thresholds
Surface Roughness	Good: below 10 Average: between 10 and 20 Bad: above 30
Shore D Hardness	Good: above 60 Average: between 50 and 60 Bad: below 50
Tensile Strength	Good: above 45 Average: between 40 and 45 Bad: below 40

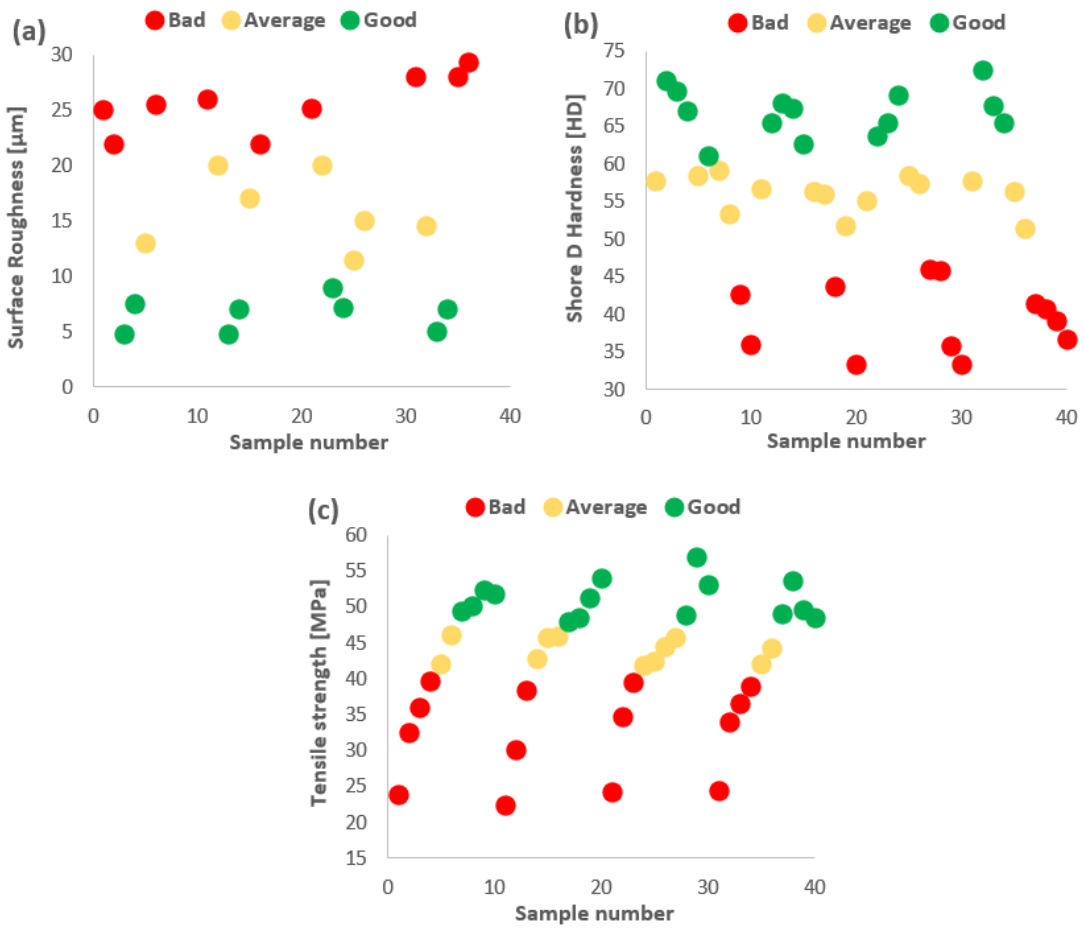


Figure 16. Categorisation results: (**a**) Surface roughness; (**b**) Shore D hardness; (**c**) Tensile strength.

Using the simulation results from the ROM, the corresponding extrusion temperature profile for each sample was generated. The entire 3D mesh of node temperature values from the microchannel simulations was turned into a 1D normalized array (based on the inlet temperature) and used as the input for the machine learning algorithms. Using the machine learning algorithms (Section 3.5), the simulation data was linked to the final category of

each part (Table 9; Figure 16) to generate the database. The ratio between the training data and the test data was 80% to 20%. Figure 17 shows the model accuracy comparison between the two algorithms for the three parameters (surface roughness, shore D hardness, and tensile strength), with accuracy R2 %, mean squared error % (MSE), and mean absolute error % (MAE).

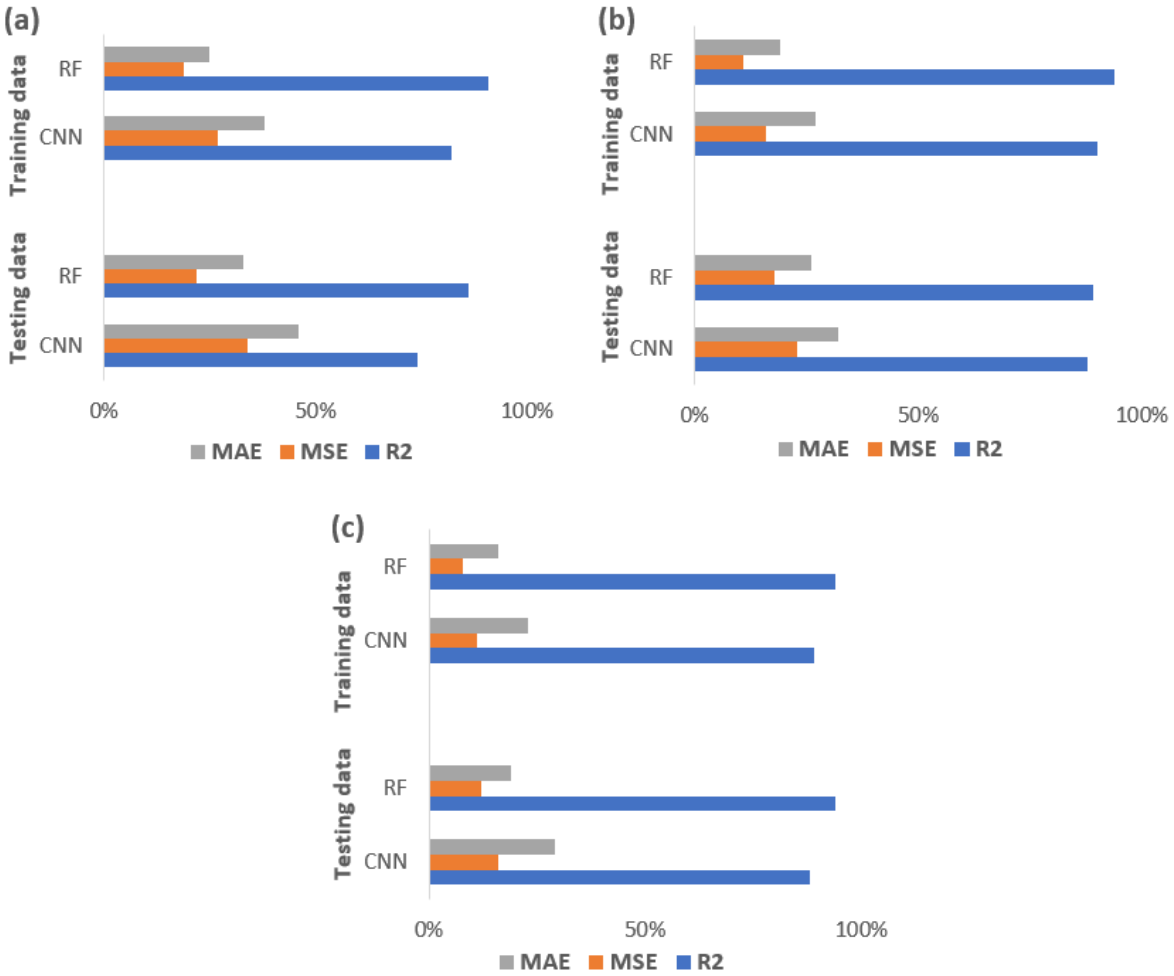


Figure 17. Comparison between convolutional neural network and random forest; (**a**) Surface roughness; (**b**) Shore D hardness; (**c**) Tensile strength.

It can be seen from the testing data for the surface roughness in Figure 17a that the accuracy of RF is 86%, compared to 74% for CNN. This is the same for the hardness and tensile strength testing data as well, where RF showed higher accuracy compared to CNN. The accuracy of the testing data for hardness is 89% for RF and 88% for CNN, showing a very good correlation. However, testing data for tensile strength showed a 94% accuracy for RF, compared to 88% for CNN. RF is better compared to CNN in terms of predicting the categories of the printed parts. The lower accuracy of the surface roughness test data is due to the limited number of samples as compared to hardness and tensile strength. More data could help in achieving better accuracy. Based on the results shown in Figure 17, it is evident that random forest demonstrates comparatively better results, as it is designed specifically for classification problems [31,40,42].

Additionally, Table 10 shows the confusion matrix analysis of the random forest classifier. The definitions of the metrics used are as follows [85]:

$$Accuracy = \frac{True\ positives + True\ negatives}{True\ positives + True\ negatives + False\ positives + False\ negatives}$$

$$Precision = \frac{True\ positive}{True\ positives + False\ positives}$$

$$Recall = \frac{True\ positives}{True\ positives + False\ negatives}$$

$$F1\ score = \frac{2 \times True\ positives}{2 \times True\ positives + False\ positives + False\ negatives}$$

Table 10. Confusion matrix analysis of the random forest classifier for surface roughness, hardness, and tensile strength.

Class	Total Samples	Total Positives	Accuracy	Precision	Recall	F1 Score
Surface Roughness						
Good	8	8	91.67%	0.88	0.88	0.82
Average	7	8	87.50%	0.75	0.86	0.8
Bad	9	8	87.50%	0.88	0.88	0.88
Shore D Hardness						
Good	14	13	92.50%	0.92	0.86	0.89
Average	14	15	92.50%	0.87	0.93	0.9
Bad	12	12	95.00%	0.92	0.92	0.92
Tensile Strength						
Good	15	14	97.50%	1	0.93	0.97
Average	11	12	92.50%	0.83	0.91	0.87
Bad	14	14	95.00%	0.93	0.93	0.93

The statistical metrics of the confusion matrix clearly highlight the accuracy and reliability of using machine learning analysis in correlating the output of the digital twin to the experimental data. The combination of reduced order modelling and machine learning can analyse the simulation results and establish the correlation to the experimental data with high accuracy.

5. Conclusions

FFF is a commonly used AM method and requires optimisation of its process parameters to achieve the desired results. Even the same material from different vendors can produce varied results using the same process parameters or 3D printer. Therefore, it is imperative to mitigate the effects of the trial-and-error approach and develop a methodology that can help in identifying the optimal process parameters for the FFF process to produce the desired results in the printed parts. This paper presents a combinational approach of a validated digital twin and machine learning algorithms to correlate the process parameters of the FFF process with the properties of the printed PLA parts. Two input parameters have been used in this work, i.e., material extrusion rates (70% to 160%) and extrusion temperatures (180 °C to 210 °C). The quality of the printed PLA parts is characterised using surface roughness, hardness, and tensile strength. To achieve this correlation, a digital twin of the extruder assembly, including its PID/PWM control circuit, has been modelled using ANSYS Twin Builder. The output from the digital twin is a set of simulations that represent the intricacies of the printing process for each sample. The simulations generated by the extruder assembly twin builder have been validated against experimental data and show a good agreement for PLA. As per the input parameters, five samples of each configuration were printed and experimentally tested for surface roughness, hardness, and tensile strength in accordance with British and International standards. Like the experimental data for the input combinations, simulation data from the digital twin is also required. These two datasets are needed to train the machine learning algorithms to establish a correlation between the input and output parameters. To develop the larger system of simulations from the digital twin, a reduced order model was developed. This is required to complement

the experimental database to be used by the machine learning algorithms. The correlation was established by training two such algorithms (i.e., convolutional neural network and random forest classifier) on the combined database (comprising experimental data and simulation output). The results show that the CNN has an accuracy range of 74% to 88% compared to the higher range of 88% to 95% of RF for the testing data of the three output parameters (i.e., surface roughness, shore D hardness, and tensile strength).

The digital twin scheme coupled with the use of machine learning presented in this study can be used for any FFF material, extruder assembly, user specified temperature, feed rate, and infill extrusion/flow rate. This methodology can help in saving considerable amount of time and resources as well as limiting the use of trial-and-error methods to identify the optimal process parameters for a material to achieve the desired results in a product.

Author Contributions: Conceptualization, J.B.; methodology, J.B.; investigation, J.B.; validation J.B and V.M.; formal analysis J.B. and V.M.; resources, J.B. and V.M.; data curation, J.B. and V.M.; writing—original draft preparation, J.B. and V.M.; writing—review and editing, J.B.; project administration, J.B. All authors have read and agreed to the published version of the manuscript.

Funding: This research received no external funding.

Data Availability Statement: The data used in this research work can be made available upon request.

Conflicts of Interest: The authors declare no conflict of interest.

Nomenclature

Symbol	Description	Symbol	Description
C_μ, $C_{\omega 1}$, $C_{\omega 2}$	Turbulent constants	$\Delta P(Q)$	Rise in pressure across the fan for a given axial flow rate Q
C	Specific heat	h	Thickness of the toroid region swept by the blades in the axial direction
ρ	Density	W_{fan}	Fan power
u	Velocity vector component	r	Local radial distance from the fan axis
x	Direction vector component	$\Omega_{operating}$	Fan operating angular velocity
P	Pressure	R_h	Radius of the fan hub
τ	Stress tensor component	R_{ip}	Radius of a point on the fan blade based on the inflection point ratio
g	Gravitational acceleration	R_t	Radius of the fan blade tip
δ	Kronecker delta	ρ	Fluid density
i, j, k	Rotating directional suffixes	V_Φ	Local tangential velocity
T	Temperature	λ	Thermal conductivity
k	Turbulence kinetic energy	ε	Specific rate of dissipation
t	Time	μ	Viscosity
μ_t	Turbulence viscosity	v_t	Kinematic turbulent viscosity
u_m	Velocity vector component mean (time averaged)	H	Enthalpy
h_{ref}	Reference enthalpy	T_{ref}	Reference temperature
L	Latent heat of melting	T_l	Liquidus temperature
T_s	Solidus temperature	A_{mush}	Mushy zone constant
η	Cross-WLF viscosity	η_0	zero shear viscosity
$\dot{\gamma}$	Shear rate	τ^*	Critical stress level
K_p	Proportional gain	K_i	Integration gain
K_d	Differential gain	T_i	Rest time
T_d	Rate time	$K(\varphi)$	Stiffness matrix
χ	System variable	Φ	Basis functions
inf_r	Infill flow	D_s	Deposition speed
h	Layer height	w	Line width

References

1. Beaman, J.J.; Bourell, D.L.; Seepersad, C.C.; Kovar, D. Additive manufacturing review: Early past to current practice. *J. Manuf. Sci. Eng.* **2020**, *142*, 110812. [CrossRef]
2. Kumar, M.B.; Sathiya, P. Methods and materials for additive manufacturing: A critical review on advancements and challenges. *Thin-Walled Struct.* **2021**, *159*, 107228. [CrossRef]
3. Butt, J.; Oxford, P.; Sadeghi-Esfahlani, S.; Ghorabian, M.; Shirvani, H. Hybrid manufacturing and mechanical characterization of Cu/PLA composites. *Arab. J. Sci. Eng.* **2020**, *45*, 9339–9356. [CrossRef]
4. Butt, J.; Mebrahtu, H.; Shirvani, H. Tensile lap-shear and flexural behaviour of aluminium metal foil parts made by composite metal foil manufacturing. *Prog. Addit. Manuf.* **2019**, *4*, 73–81. [CrossRef]
5. Xia, C.; Pan, Z.; Polden, J.; Li, H.; Xu, Y.; Chen, S. Modelling and prediction of surface roughness in wire arc additive manufacturing using machine learning. *J. Intell. Manuf.* **2022**, *33*, 1467–1482. [CrossRef]
6. Parandoush, P.; Lin, D. A review on additive manufacturing of polymer-fiber composites. *Compos. Struct.* **2017**, *182*, 36–53. [CrossRef]
7. Butt, J.; Mebrahtu, H.; Shirvani, H. Microstructure and mechanical properties of dissimilar pure copper foil/1050 aluminium composites made with composite metal foil manufacturing. *J. Mater. Process. Technol.* **2016**, *238*, 96–107. [CrossRef]
8. Chen, H.; Zhao, Y.F. Process parameters optimization for improving surface quality and manufacturing accuracy of binder jetting additive manufacturing process. *Rapid Prototyp. J.* **2016**, *22*, 527–538. [CrossRef]
9. Chacón, J.M.; Caminero, M.A.; García-Plaza, E.; Núnez, P.J. Additive manufacturing of PLA structures using fused deposition modelling: Effect of process parameters on mechanical properties and their optimal selection. *Mater. Des.* **2017**, *124*, 143–157. [CrossRef]
10. Butt, J.; Bhaskar, R.; Mohaghegh, V. Analysing the effects of layer heights and line widths on FFF-printed thermoplastics. *Int. J. Adv. Manuf. Technol.* **2022**, *121*, 7383–7411. [CrossRef]
11. Brennan, M.C.; Keist, J.S.; Palmer, T.A. Defects in metal additive manufacturing processes. *J. Mater. Eng. Perform.* **2021**, *30*, 4808–4818. [CrossRef]
12. Oliveira, J.P.; LaLonde, A.D.; Ma, J. Processing parameters in laser powder bed fusion metal additive manufacturing. *Mater. Des.* **2020**, *193*, 108762. [CrossRef]
13. Yakout, M.; Cadamuro, A.; Elbestawi, M.A.; Veldhuis, S.C. The selection of process parameters in additive manufacturing for aerospace alloys. *Int. J. Adv. Manuf. Technol.* **2017**, *92*, 2081–2098. [CrossRef]
14. Butt, J.; Mebrahtu, H.; Shirvani, H. Numerical and experimental analysis of product development by composite metal foil manufacturing. *Int. J. Rapid Manuf.* **2018**, *7*, 59–82. [CrossRef]
15. Forés-Garriga, A.; Pérez, M.A.; Gómez-Gras, G.; Reyes-Pozo, G. Role of infill parameters on the mechanical performance and weight reduction of PEI Ultem processed by FFF. *Mater. Des.* **2020**, *193*, 108810. [CrossRef]
16. Gao, J. Production of multiple material parts using a desktop 3D printer. In *Advances in Manufacturing Technology XXXI: Proceedings of the 15th International Conference on Manufacturing Research, Incorporating the 32nd National Conference on Manufacturing Research, University of Greenwich, London, UK, 5–7 September 2017*; IOS Press: Amsterdam, The Netherlands, 2017; Volume 6, p. 148.
17. Butt, J.; Bhaskar, R.; Mohaghegh, V. Investigating the effects of extrusion temperatures and material extrusion rates on FFF-printed thermoplastics. *Int. J. Adv. Manuf. Technol.* **2021**, *117*, 2679–2699. [CrossRef]
18. Liao, J.; Shen, Z.; Xiong, G.; Liu, C.; Luo, C.; Lu, J. Preliminary study on fault diagnosis and intelligent learning of fused deposition modeling (FDM) 3D Printer. In Proceedings of the 2019 14th IEEE Conference on Industrial Electronics and Applications (ICIEA), Xi'an, China, 19–21 June 2019; pp. 2098–2102.
19. Fico, D.; Rizzo, D.; Casciaro, R.; Esposito Corcione, C. A review of polymer-based materials for Fused Filament Fabrication (FFF): Focus on sustainability and recycled materials. *Polymers* **2022**, *14*, 465. [CrossRef]
20. Maurizi, M.; Slavič, J.; Cianetti, F.; Jerman, M.; Valentinčič, J.; Lebar, A.; Boltežar, M. Dynamic measurements using FDM 3D-printed embedded strain sensors. *Sensors* **2019**, *19*, 2661. [CrossRef]
21. Holzmond, O.; Li, X. In situ real time defect detection of 3D printed parts. *Addit. Manuf.* **2017**, *17*, 135–142. [CrossRef]
22. Tlegenov, Y.; Hong, G.S.; Lu, W.F. Nozzle condition monitoring in 3D printing. *Robot. Comput.-Integr. Manuf.* **2018**, *54*, 45–55. [CrossRef]
23. Rao, P.K.; Liu, J.P.; Roberson, D.; Kong, Z.J.; Williams, C. Online real-time quality monitoring in additive manufacturing processes using heterogeneous sensors. *J. Manuf. Sci. Eng.* **2015**, *137*, 061007. [CrossRef]
24. Tichý, T.; Šefl, O.; Veselý, P.; Dušek, K.; Bušek, D. Mathematical modelling of temperature distribution in selected parts of fff printer during 3d printing process. *Polymers* **2021**, *13*, 4213. [CrossRef] [PubMed]
25. Ramos, N.; Mittermeier, C.; Kiendl, J. Experimental and numerical investigations on heat transfer in fused filament fabrication 3D-printed specimens. *Int. J. Adv. Manuf. Technol.* **2022**, *118*, 1367–1381. [CrossRef]
26. Phan, D.D.; Horner, J.S.; Swain, Z.R.; Beris, A.N.; Mackay, M.E. Computational fluid dynamics simulation of the melting process in the fused filament fabrication additive manufacturing technique. *Addit. Manuf.* **2020**, *33*, 101161. [CrossRef]
27. Zhu, Q.; Liu, Z.; Yan, J. Machine learning for metal additive manufacturing: Predicting temperature and melt pool fluid dynamics using physics-informed neural networks. *Comput. Mech.* **2021**, *67*, 619–635. [CrossRef]
28. Meng, L.; McWilliams, B.; Jarosinski, W.; Park, H.Y.; Jung, Y.G.; Lee, J.; Zhang, J. Machine learning in additive manufacturing: A review. *Jom* **2020**, *72*, 2363–2377. [CrossRef]

29. Wang, C.; Tan, X.P.; Tor, S.B.; Lim, C.S. Machine learning in additive manufacturing: State-of-the-art and perspectives. *Addit. Manuf.* **2020**, *36*, 101538. [CrossRef]
30. Valizadeh, M.; Wolff, S.J. Convolutional Neural Network applications in additive manufacturing: A review. *Adv. Ind. Manuf. Eng.* **2022**, *4*, 100072. [CrossRef]
31. Jayasudha, M.; Elangovan, M.; Mahdal, M.; Priyadarshini, J. Accurate Estimation of Tensile Strength of 3D Printed Parts Using Machine Learning Algorithms. *Processes* **2022**, *10*, 1158. [CrossRef]
32. Zheng, P.; Sivabalan, A.S. A generic tri-model-based approach for product-level digital twin development in a smart manufacturing environment. *Robot. Comput.-Integr. Manuf.* **2020**, *64*, 101958. [CrossRef]
33. Pantelidakis, M.; Mykoniatis, K.; Liu, J.; Harris, G. A digital twin ecosystem for additive manufacturing using a real-time development platform. *Int. J. Adv. Manuf. Technol.* **2022**, *120*, 6547–6563. [CrossRef] [PubMed]
34. Stark, R.; Fresemann, C.; Lindow, K. Development and operation of Digital Twins for technical systems and services. *CIRP Ann.* **2019**, *68*, 129–132. [CrossRef]
35. Gunasegaram, D.R.; Murphy, A.B.; Matthews, M.J.; DebRoy, T. The case for digital twins in metal additive manufacturing. *J. Phys. Mater.* **2021**, *4*, 040401. [CrossRef]
36. Mukherjee, T.; DebRoy, T. A digital twin for rapid qualification of 3D printed metallic components. *Appl. Mater. Today* **2019**, *14*, 59–65. [CrossRef]
37. Kumar, S.; Kolekar, T.; Patil, S.; Bongale, A.; Kotecha, K.; Zaguia, A.; Prakash, C. A Low-Cost Multi-Sensor Data Acquisition System for Fault Detection in Fused Deposition Modelling. *Sensors* **2022**, *22*, 517. [CrossRef]
38. Alejandrino, J.D.; Concepcion, R.S., II; Lauguico, S.C.; Tobias, R.R.; Venancio, L.; Macasaet, D.; Bandala, A.A.; Dadios, E.P. A machine learning approach of lattice infill pattern for increasing material efficiency in additive manufacturing processes. *Int. J. Mech. Eng. Robot. Res.* **2020**, *9*, 1253–1263. [CrossRef]
39. Banadaki, Y.; Razaviarab, N.; Fekrmandi, H.; Sharifi, S. Toward enabling a reliable quality monitoring system for additive manufacturing process using deep convolutional neural networks. *arXiv* **2020**, arXiv:2003.08749.
40. Wu, D.; Wei, Y.; Terpenny, J. Predictive modelling of surface roughness in fused deposition modelling using data fusion. *Int. J. Prod. Res.* **2019**, *57*, 3992–4006. [CrossRef]
41. Hooda, N.; Chohan, J.S.; Gupta, R.; Kumar, R. Deposition angle prediction of Fused Deposition Modeling process using ensemble machine learning. *ISA Trans.* **2021**, *116*, 121–128. [CrossRef]
42. Barrios, J.M.; Romero, P.E. Decision tree methods for predicting surface roughness in fused deposition modeling parts. *Materials* **2019**, *12*, 2574. [CrossRef]
43. Mourtzis, D.; Togias, T.; Angelopoulos, J.; Stavropoulos, P. A Digital Twin architecture for monitoring and optimization of Fused Deposition Modeling processes. *Procedia CIRP* **2021**, *103*, 97–102. [CrossRef]
44. Balta, E.C.; Tilbury, D.M.; Barton, K. A digital twin framework for performance monitoring and anomaly detection in fused deposition modeling. In Proceedings of the 2019 IEEE 15th International Conference on Automation Science and Engineering (CASE), Vancouver, BC, Canada, 22–26 August 2019; pp. 823–829.
45. Osho, J.; Hyre, A.; Pantelidakis, M.; Ledford, A.; Harris, G.; Liu, J.; Mykoniatis, K. Four Rs Framework for the development of a digital twin: The implementation of Representation with a FDM manufacturing machine. *J. Manuf. Syst.* **2022**, *63*, 370–380. [CrossRef]
46. Corradini, F.; Silvestri, M. Design and testing of a digital twin for monitoring and quality assessment of material extrusion process. *Addit. Manuf.* **2022**, *51*, 102633. [CrossRef]
47. *BS EN ISO 527-2:2012*; Plastics—Determination of Tensile Properties—Part 2: Test Conditions for Moulding and Extrusion Plastics. British, European and International Standard: London, UK, 2012.
48. PrimaValue™ PLA. Available online: https://primacreator.com/collections/pla (accessed on 14 September 2022).
49. Ultimaker Cura: Advanced 3D Printing Software, Made Accessible. Available online: https://ultimaker.com/en/products/ultimaker-cura-software (accessed on 14 October 2022).
50. Meshram, P.M.; Kanojiya, R.G. Tuning of PID controller using Ziegler-Nichols method for speed control of DC motor. In Proceedings of the IEEE—International Conference on Advances in Engineering, Science and Management (ICAESM-2012), Nagapattinam, India, 30–31 March 2012; pp. 117–122.
51. Aisuwarya, R.; Hidayati, Y. Implementation of ziegler-nichols PID tuning method on stabilizing temperature of hot-water dispenser. In Proceedings of the 2019 16th International Conference on Quality in Research (QIR): International Symposium on Electrical and Computer Engineering, Padang, Indonesia, 22–24 July 2019; pp. 1–5.
52. Lin, C.N. Enhanced heat transfer performance of cylindrical surface by piezoelectric fan under forced convection conditions. *Int. J. Heat Mass Transf.* **2013**, *60*, 296–308. [CrossRef]
53. Roe, B.; Jaiman, R.; Haselbacher, A.; Geubelle, P.H. Combined interface boundary condition method for coupled thermal simulations. *Int. J. Numer. Methods Fluids* **2008**, *57*, 329–354. [CrossRef]
54. Peng, W.; Li, G.; Geng, J.; Yan, W. An iterative correction method for the input fan curve in an actuator disk model. *Int. J. Vent.* **2018**, *17*, 240–255. [CrossRef]
55. Mukherjee, T.; Wei, H.L.; De, A.; DebRoy, T. Heat and fluid flow in additive manufacturing—Part II: Powder bed fusion of stainless steel, and titanium, nickel and aluminum base alloys. *Comput. Mater. Sci.* **2018**, *150*, 369–380. [CrossRef]

56. Bergström, J.S.; Hayman, D. An overview of mechanical properties and material modeling of polylactide (PLA) for medical applications. *Ann. Biomed. Eng.* **2016**, *44*, 330–340. [CrossRef]
57. Anyanwu, I.S.; Hou, Y.; Xi, F.; Wang, X.; Yin, Y.; Du, Q.; Jiao, K. Comparative analysis of two-phase flow in sinusoidal channel of different geometric configurations with application to PEMFC. *Int. J. Hydrogen Energy* **2019**, *44*, 13807–13819. [CrossRef]
58. John, B.; Senthilkumar, P.; Sadasivan, S. Applied and theoretical aspects of conjugate heat transfer analysis: A review. *Arch. Comput. Methods Eng.* **2019**, *26*, 475–489. [CrossRef]
59. Fawzy, H.; Zheng, Q.; Jiang, Y.; Lin, A.; Ahmad, N. Conjugate heat transfer of impingement cooling using conical nozzles with different schemes in a film-cooled blade leading-edge. *Appl. Therm. Eng.* **2020**, *177*, 115491. [CrossRef]
60. Mori, K.; Yamashita, S.; Fukuda, T.; Sekiguchi, M.; Ezawa, H.; Akejima, S. 3D Fan-Out Package Technology with Photosensitive Through Mold Interconnects. In Proceedings of the 2019 IEEE 69th Electronic Components and Technology Conference (ECTC), Las Vegas, NV, USA, 28–31 May 2019; pp. 1140–1145.
61. Ebrahimi, A.; Kleijn, C.R.; Richardson, I.M. Sensitivity of numerical predictions to the permeability coefficient in simulations of melting and solidification using the enthalpy-porosity method. *Energies* **2019**, *12*, 4360. [CrossRef]
62. Kim, S.Y.; Park, S.H. Identification of Cross-WLF Viscosity Model Parameters Using Optimization Technique. *J. Korea Acad. Ind. Coop. Soc.* **2018**, *19*, 623–632.
63. Baines, M.J.; Hubbard, M.E.; Jimack, P.K. Velocity-based moving mesh methods for nonlinear partial differential equations. *Commun. Comput. Phys.* **2011**, *10*, 509–576. [CrossRef]
64. Özkan, F.; Wenka, A.; Hansjosten, E.; Pfeifer, P.; Kraushaar-Czarnetzki, B. Numerical investigation of interfacial mass transfer in two phase flows using the VOF method. *Eng. Appl. Comput. Fluid Mech.* **2016**, *10*, 100–110. [CrossRef]
65. Lehmann, M.; Gekle, S. Analytic solution to the piecewise linear interface construction problem and its application in curvature calculation for volume-of-fluid simulation codes. *Computation* **2022**, *10*, 21. [CrossRef]
66. Lei, M.; Wei, Q.; Li, M.; Zhang, J.; Yang, R.; Wang, Y. Numerical Simulation and Experimental Study the Effects of Process Parameters on Filament Morphology and Mechanical Properties of FDM 3D Printed PLA/GNPs Nanocomposite. *Polymers* **2022**, *14*, 3081. [CrossRef]
67. Test Equipment Solutions. Available online: https://www.testequipmenthq.com/product/lecroy-waverunner-204xi (accessed on 14 September 2022).
68. TELEDYNE FLIR. Available online: https://www.flir.eu/products/c5/ (accessed on 14 September 2022).
69. Omni Instruments. Available online: https://www.omniinstruments.co.uk/datataker-dt80-data-logger.html (accessed on 16 September 2022).
70. Park, Y.J.; Yu, T.; Yim, S.J.; You, D.; Kim, D.P. A 3D-printed flow distributor with uniform flow rate control for multi-stacked microfluidic systems. *Lab Chip* **2018**, *18*, 1250–1258. [CrossRef]
71. Mitutoyo: Surftest SJ-210 [inch/mm]. Available online: https://www.mitutoyo.com/webfoo/wp-content/uploads/J_section.pdf (accessed on 16 September 2022).
72. *ISO 21920–2:2021*; Geometrical Product Specifications (GPS)—Surface Texture: Profile—Part 2: Terms, Definitions and Surface Texture Parameters. British, European and International Standard: London, UK, 2021.
73. *ISO I (2003) 868:2003*; Plastics and Ebonite–Determination of Indentation Hardness by Means of a Durometer (Shore Hardness). International Organization for Standardization: Geneva, Switzerland, 2003.
74. Kerfriden, P.; Ródenas, J.J.; Bordas, S.A. Certification of projection-based reduced order modelling in computational homogenisation by the constitutive relation error. *Int. J. Numer. Methods Eng.* **2014**, *97*, 395–422. [CrossRef]
75. Kim, J.G.; Lee, P.S. An enhanced craig–bampton method. *Int. J. Numer. Methods Eng.* **2015**, *103*, 79–93. [CrossRef]
76. Michiels, W.; Jarlebring, E.; Meerbergen, K. Krylov-based model order reduction of time-delay systems. *SIAM J. Matrix Anal. Appl.* **2011**, *32*, 1399–1421. [CrossRef]
77. Albawi, S.; Mohammed, T.A.; Al-Zawi, S. Understanding of a convolutional neural network. In Proceedings of the 2017 International Conference on Engineering and Technology (ICET), Antalya, Turkey, 21–23 August 2017; pp. 1–6.
78. Belgiu, M.; Drăguţ, L. Random forest in remote sensing: A review of applications and future directions. *ISPRS J. Photogramm. Remote Sens.* **2016**, *114*, 24–31. [CrossRef]
79. Ma, H.; Zhang, Y.; Thuerey, N.; Hu, X.; Haidn, O.J. Physics-driven Learning of the Steady Navier-Stokes Equations using Deep Convolutional Neural Networks. *arXiv* **2021**, arXiv:2106.09301. [CrossRef]
80. Nasiri, S.; Khosravani, M.R. Machine learning in predicting mechanical behavior of additively manufactured parts. *J. Mater. Res. Technol.* **2021**, *14*, 1137–1153. [CrossRef]
81. Al Amrani, Y.; Lazaar, M.; El Kadiri, K.E. Random forest and support vector machine based hybrid approach to sentiment analysis. *Procedia Comput. Sci.* **2018**, *127*, 511–520. [CrossRef]
82. Ramadan, K.M.; Kamil, M.; Tlili, I.; Qisieh, O. Analysis of thermal creep effects on fluid flow and heat transfer in a microchannel gas heating. *J. Therm. Sci. Eng. Appl.* **2021**, *13*, 061011. [CrossRef]
83. Li, W.Q.; Qu, Z.G.; He, Y.; Tao, W. Experimental and numerical studies on melting phase change heat transfer in open-cell metallic foams filled with paraffin. *Appl. Therm. Eng.* **2012**, *37*, 1–9. [CrossRef]

84. Le, T.T. Prediction of tensile strength of polymer carbon nanotube composites using practical machine learning method. *J. Compos. Mater.* **2021**, *55*, 787–811. [CrossRef]
85. Yacouby, R.; Axman, D. Probabilistic extension of precision, recall, and F1 score for more thorough evaluation of classification models. In Proceedings of the First Workshop on Evaluation and Comparison of NLP Systems, Online, 20 November 2020; pp. 79–91.

Disclaimer/Publisher's Note: The statements, opinions and data contained in all publications are solely those of the individual author(s) and contributor(s) and not of MDPI and/or the editor(s). MDPI and/or the editor(s) disclaim responsibility for any injury to people or property resulting from any ideas, methods, instructions or products referred to in the content.